Analytical Model to Predict Axial Stress-strain Behavior of Heat-damaged Unreinforced Concrete Columns Wrapped by FRP Jacket

Javad Shayanfar [1], Joaquim A. O. Barros [2] and Mohammadali Rezazadeh [3]

[1] PhD Candidate, ISISE, Department of Civil Engineering, University of Minho, Azurém 4800-058 Guimarães, Portugal, id8287@alunos.uminho.pt (corresponding author)

[2] Full Prof., ISISE, IBS, Department of Civil Engineering, University of Minho, Azurém 4800-058 Guimarães, Portugal, barros@civil.uminho.pt

[3] Lecturer, Civil Eng., Department of Mechanical and Construction Engineering, Northumbria University, Newcastle upon Tyne, NE1 8ST, United Kingdom, mohammadali.rezazadeh@northumbria.ac.uk

Abstract:

Although there are several confinement models to obtain analytically the axial stress-strain response ($f_c - \varepsilon_c$) of concrete columns wrapped with fiber-reinforced-polymer (FRP) jacket at ambient conditions, a reliable design-oriented model to determine the $f_c - \varepsilon_c$ of heat-damaged concrete columns post-confined with FRP is still lacking in the literature. This study aims to address this research gap, by proposing a formulation that predicts the favourable effects of FRP confinement on concrete elements previously exposed to high temperatures. This model proposes a closed-form formulation to derive a $f_c - \varepsilon_c$ expression, including a set of strength and strain sub-models to calculate the stress/strain information at transition and ultimate points defining the stress-strain response. To develop the model and calibrate its key components by data analysis of statistical treatment techniques, a large test database of FRP confined unheated/heat-damaged concrete of circular/square cross-section consisting of 1914 specimens was collected. The proposed design-oriented model is able to demonstrate the influence of pre-existing thermal damage on the axial $f_c - \varepsilon_c$ relationship, whose reliability is revealed comprehensively through predicting data from several experimental heat-damaged concrete specimens confined with FRP systems.

Keywords: FRP confinement; heat-damaged concrete; Axial behavior; Stress-strain model

1- Introduction

Post-fire experimental research has demonstrated that at fire occurrence, the mechanical, chemical, and physical characteristics of concrete exposed to high temperatures are deteriorated, leading to concrete dehydration, higher porous microstructure and decrease of the bond between concrete constituents,, resulting in stiffness and strength degradation (Kodur [1] and Bamonte and Monte [2]). Accordingly, the response of a concrete structure in terms of its serviceability, seismic performance and durability is influenced noticeably when subjected to high temperatures (Demir *et al.* [3]). Considering the relatively high cost of reconstruction alternative, the usage of a post-fire strengthening solution for assuring the required performance and strength capacity level of a fire damaged concrete structure can be justified. Experimental researches [4-8] have evidenced the potentialities of fiber-reinforced-polymer (FRP)-based confinement technique for improving the axial strength, ductility and stiffness of heat-damaged concrete columns.

Many experimental research studies have been carried out for assessing the influence of FRP confinement on the axial and dilation responses of concrete columns of circular/non-circular cross section at room temperature subjected to axial loading [9-12]. For the case of FRP confined circular concrete (FCCC), Eid *et al.* [9] experimentally demonstrated that the FRP confinement effectiveness decreases with the increase of the concrete strength class. Shan *et al.* [12] performed axial compressive loading tests on FRP confined square concrete (FCSC) with various lengths of corner radius (r). The experimental results revealed that by transforming the column shape from a circular cross-section to a square cross-section with sharp corners, the FRP confining effectiveness, in terms of axial strength and deformability, decreases noticeably, which is known as shape effect. Nevertheless, available literature shows that experimental studies on the utilization of FRP confinement to repair heat-damaged concrete specimens under axial loading are still limited. Bisby *et al.* [4] executed axial

compression tests on FRP confined heat-damaged circular concrete (FCHCC) subjected to different maximum exposure temperatures (T_m as shown in Fig. 1). The results showed that the axial and dilation responses of heat-damaged concrete columns are significantly improved by using FRP full confinement system, demonstrating its reliability. Furthermore, at a certain T_m, the loss in terms of axial stiffness is more significant for heat-damaged concrete specimens exposed to longer temperature exposure duration. Lenwari *et al.* [5] experimentally evaluated the effects of the influential factors in confinement-induced enhancements of FCHCC, including the compressive strength of unconfined concrete, maximum exposure temperature, exposure duration and the method of cooling regime. It was verified that the enhancements offered by FRP confining system imposed to heat-damaged concrete specimens (FCHCC) were more pronounced for ones having higher concrete strength. Furthermore, by the application of water-cooled method for cooling regime of heat-exposed specimens, in comparison with air-cooled method, less compressive strength of FCHCC was obtained. Ouyang *et al.* [6] experimentally demonstrated that by increasing T_m, the magnitude of axial strength enhancement (the ratio of axial strengths of confined and unconfined heat-damaged concrete) induced by FRP confinement increases, as also evidenced experimentally by Song *et al.* [7] for the case of FRP confined heat-damaged square concrete (FCHSC).

In order to predict the stress–strain response of FRP confined concrete under ambient temperatures, many models have been proposed, generally categorized in two groups: analysis-oriented models, AOM, ([13-16) and design-oriented models, DOM, ([17-21]). The AOM determines the axial stress at a given level of axial strain, based on the relationship between FRP confinement pressure and axial strain obtained from a dilation model, through an incremental/iterative calculation procedure, which might not be proper for direct use in design practice. The DOM determines the complete axial stress-strain response through adopting a formulation that couples a simple stress-strain base equation with stress/strain information at

the transition point (f_{ctr} and ε_{ctr}) and at the ultimate stage (f_{cu} and ε_{cu}), see Fig. 1c. Lam and Teng [17] proposed a DOM for FCCC (FRP fully confined columns of circular cross section) at room temperature in which the values of f_{cu} and ε_{cu} are required as input parameters. For this purpose, formulations were derived based on a test database of FCCC. In fact, Teng *et al.* [19] presented a refined version of Lam and Teng [17]'s model by improving expressions with a better correlation with experimental data of a larger database. Fallahpour *et al.* [21] developed a new DOM in which, in addition to the evaluation of f_{cu} and ε_{cu}, simple formulations were suggested to obtain f_{ctr} and ε_{ctr} as input parameters. In general, for FRP fully confined concrete with square cross-section (FCSC) at room temperature, the following approaches are adopted to reflect the substantial influence of the shape effect on the confinement-induced improvements: i) addressing theoretically the arching action phenomenon based on the concept of confinement efficiency factor (Mander *et al.* [22] and Lam and Teng [18] and Shayanfar *et al.* [23]); ii) addressing empirically based on statistical analysis performed on a series of test dada (Wei and Wu [20], Cao *et al.* [24] and Shayanfar *et al.* [25]).

Bisby *et al.* [4] generalized ACI 440.2R-08 [26]'s model, which was developed exclusively for FCCC at ambient condition, in an attempt of predicting the axial stress-strain response of FCHCC (at high temperatures). In this model, for the sake of simplicity, the effectiveness/capability of FRP confinement in improving concrete behavior was assumed identical for concrete at ambient and elevated condition. In other words, the axial strength and strain enhancements induced by confinement on FCHCC were considered the same adopted on FCCC at ambient condition. The generalized model has predicted conservative values regarding the corresponding experimental results. Ouyang *et al.* [6] assessed the applicability of existing confinement models (Lam and Teng [17], and Ozbakkaloglu and Lim [27]), which were developed exclusively for FCCC at ambient condition, to be generalized for FCHCC

through addressing the mechanical characteristics of unconfined heat-damaged concrete. They evidenced that these generalized models predict conservatively the axial response of experimentally tested FCHCC specimens, which was also demonstrated by Song *et al.* [7] for FCHSC.

In this paper, a new generalized DOM is developed to predict a stress-strain relation ($f_c - \varepsilon_c$) of heat-damaged circular/square concrete element fully confined with FRP. This model consists of a closed-form formulation to derive a $f_c - \varepsilon_c$ relationship, which integrates a set of strength and strain sub-models to calculate the stress/strain information at the transition and ultimate points. To calibrate the stress-strain model and its sub-models based on regression analysis method of statistical treatment technique, a large test database of 1914 specimens consisting 1517 FCCC, 256 FCSC, 109 FCHCC, and 35 FCHSC specimens was collected. The initial focus is placed on the determination of the $f_c - \varepsilon_c$ expression including parabolic and linear functions based on experimental observations of axial response of FCHCC/FCHSC with different levels of pre-existing thermal-induced damage. Subsequently, predictive formulations are proposed to calculate stress/strain information at the transition and ultimate stages where the influences of non-circularity and thermal damage level on confinement-induced enhancements are reflected in their determination based on regression analysis. The establishment/calibration reliability of the proposed DOM for accurately predicting the influence of pre-existing thermal damage on the axial stress-strain response of FCHCC/FCHSC is demonstrated.

2- Proposed Stress-strain Model

This section is dedicated to describe the developed stress-strain based model for heat-damaged concrete confined by FRP jacket.

The key principle in FRP confinement mechanism imposed to a concrete column is that concrete dilation under axial compression generates/activates FRP confining stresses pressure, which, conversely, is able to restrict the tendency of the concrete to abruptly expand, dependent on confinement stiffness. Accordingly, besides dilation behavior, a certain level of enhancements caused by FRP confinement in terms of axial response of FRP confined concrete (FCCC/FCSC) can be assumed, as confirmed experimentally by [9-12].

However, based on the experimental studies (i.e. [4-7]), the transverse expansibility of FRP confined heat-damaged concrete (FCHCC/FCHSC) is different from that associated with unheated one, dependent on the level of thermal-induced damage. For specimens submitted to an exposure temperature up to almost 400 °C, the expansive nature of the outer surface layer leads to an earlier activation of FRP confinement pressure imposed to heat–damaged concrete columns. Consequently, the effectiveness of FRP confinement strategy in terms of initial axial stiffness and maximum compressive strength is more pronounced for heat–damaged concrete than unheated one, strongly dependent on thermal damage level. Despite these FRP confinement-induced improvements, the likelihood of FRP hoop rupture at a relatively low level of axial deformation increases by exposure temperature, resulting in a reduction in terms of axial strain ductility of FCHCC/FCHSC compared to FCCC/FCSC ([4-7]). Beyond the exposure temperature of 400 °C, Shayanfar *et al.* [28] demonstrated that as a consequence of the degeneration of micro- into meso- and macro-cracks, thermal-induced damage leads to a noticeable increase of the axial deformation of FCHCC/FCHSC. Hence, axial response of FCHCC/FCHSC converts from a parabolic-linear stress-strain relation into an almost linear one, by increasing exposure temperature.'

In order to determine the axial stress-strain relation of FCHCC/FCHSC, Bisby *et al.* [4] recommended some modifications, based on experimental observations, implemented on ACI

440.2R-08 [26]'s model to generalize it for heat-damaged concrete cases. To evaluate the performance of the generalized ACI 440.2R-08 [26]'s model to predict the stress-strain curves of FCHCC, the results obtained from this model with those measured experimentally are compared in Fig. 2. The studied case is a series of stress-strain relations obtained from axial compression tests performed on FRP confined heat-damaged concrete specimens, carried out by Ouyang *et al.* [6]. The cylinder specimens had 150 mm diameter and 300 mm height. The compressive strength of unconfined concrete was reported as 45.1 MPa. The test specimens were confined by two FRP layers. The nominal thickness of each layer was reported as 0.121 mm. Based on a coupon test, the elasticity modulus and rupture strain of FRP jacket were determined as 108.3 GPa and 0.0218, respectively. The specimens were submitted to different maximum exposure temperatures, from 200 °C to 800 °C. Even though the generalized model has a suitable predictive performance in terms of ultimate strain capacity, it results in very conservative predictions mainly in terms of stiffness and ultimate axial load capacity of FCHCC. It can be attributed to the lack of proper reflection of the pre-existing thermal damage's influence on the increase in FRP confinement-induced enhancements of FCHCC in the model generalization process, leading to conservative results. Therefore, the present study aims to develop a generalized design-oriented model (DOM) applicable to both FCHCC/FCHSC columns based on the relation between pre-existing thermal damage level and confinement effectiveness.

It is noteworthy that by increasing exposure temperature from ambient to an elevated temperature, the shape of FCHCC/FCHSC's axial response converts from a parabolic-linear stress-strain relation into an almost linear one as evidenced experimentally by [4-7]. Accordingly, on the basis of the experimental observations, the following assumptions were considered to give an analytical stress-strain model this aforementioned feature (Fig. 3):

i) The stress–strain relation has a parabolic function nature up to the transition point (f_{ctr} and ε_{ctr}), beyond which the concrete experiences a remarkable reduction in terms of axial stiffness. It can be derived analytically by a quadratic expression of f_c in the second degree of ε_c variable, in which $f_c = f_{ctr}$ at $\varepsilon_c = \varepsilon_{ctr}$.

ii) The stress–strain relation between the transition (ε_{ctr} , f_{ctr}) and ultimate stage (ε_{cu} , f_{cu}) is of linear nature (the constant line's slop is E_2).

iii) At the transition point, the first portion (parabolic function) tends to meet the straight-line second portion smoothly having an equal slop at $\varepsilon_c = \varepsilon_{ctr}$.

iv) The influence of FRP confinement on axial stress/strain enhancement at the transition and ultimate points is different. Therefore, four stress/strain sub-models are needed to address the stress/strain information at these two stages ($(\varepsilon_{ctr,T}, f_{ctr,T}), (\varepsilon_{cu,T}, f_{cu,T})$).

According to these assumptions, the first and second portions of the stress-strain curve (f_{c1}, f_{c2}) can be written by using a quadratic and a linear equation, respectively (Fig. 3):

$$f_{c1} = A_1\varepsilon_c^{\,2} + A_2\varepsilon_c + A_3 \qquad \text{for } \varepsilon_c \le \varepsilon_{ctr,T} \tag{1a}$$

$$f_{c2} = A_4\left(\varepsilon_c - \varepsilon_{ctr,T}\right) + A_5 \qquad \text{for } \varepsilon_c \ge \varepsilon_{ctr,T} \tag{1b}$$

where A_1 to A_5 are constants of the model to be determined. Due to the following conditions (based on previously indicated assumptions):

$$f_{c1}(\varepsilon_c = 0) = 0 \rightarrow A_3 = 0 \tag{2}$$

$$f_{c2}\left(\varepsilon_c = \varepsilon_{ctr,T}\right) = f_{ctr,T} \rightarrow A_5 = f_{ctr,T} \tag{3}$$

Eq. (1) is reduced to:

$$f_{c1} = A_1 \varepsilon_c^{\,2} + A_2 \varepsilon_c \qquad \text{for } \varepsilon_c \le \varepsilon_{ctr,T} \tag{4a}$$

$$f_{c2} = A_4 \left(\varepsilon_c - \varepsilon_{ctr,T} \right) + f_{ctr,T} \qquad \text{for } \varepsilon_c \ge \varepsilon_{ctr,T} \tag{4b}$$

By introducing E_2 as the slope of the straight-line of second portion, $A_4 = E_2$, Eq. (4b) is converted into:

$$f_{c2} = E_2 \left(\varepsilon_c - \varepsilon_{ctr,T} \right) + f_{ctr,T} \tag{5}$$

By applying the following constraints (that attend Assumption *iii*):

$$f_{c1}\left(\varepsilon_c = \varepsilon_{ctr,T} \right) = f_{ctr,T} \tag{6}$$

$$\frac{df_{c1}}{d\varepsilon_c}\left(\varepsilon_c = \varepsilon_{ctr,T} \right) = \frac{df_{c2}}{d\varepsilon_c}\left(\varepsilon_c = \varepsilon_{ctr,T} \right) = E_2 \tag{7}$$

it is obtained:

$$A_1 = \frac{E_2 \varepsilon_{ctr,T} - f_{ctr,T}}{\varepsilon_{ctr,T}^{\,2}} \tag{8}$$

$$A_2 = 2\frac{f_{ctr,T}}{\varepsilon_{ctr,T}} - E_2 \tag{9}$$

Once all the constraints are available, by rearranging Eq. (1), the proposed stress-strain model can be obtained from:

$$f_c = \left(2E_{ctr} - E_2 \right) \varepsilon_c - \left(\frac{E_{ctr} - E_2}{\varepsilon_{ctr,T}} \right) \varepsilon_c^{\,2} \qquad \text{for } \varepsilon_c \le \varepsilon_{ctr,T} \tag{10a}$$

$$f_c = f_{ctr,T} + E_2 \left(\varepsilon_c - \varepsilon_{ctr,T} \right) \qquad \text{for } \varepsilon_c \ge \varepsilon_{ctr,T} \tag{10b}$$

in which

$$E_{ctr} = \frac{f_{ctr,T}}{\varepsilon_{ctr,T}} \tag{11}$$

$$E_2 = \frac{f_{cu,T} - f_{ctr,T}}{\varepsilon_{cu,T} - \varepsilon_{ctr,T}} \tag{12}$$

The proposed model requires the information regarding the transition and ultimate stages ($\left(\varepsilon_{ctr,T}, f_{ctr,T}\right), \left(\varepsilon_{cu,T}, f_{cu,T}\right)$) to be able to calculate the stress-strain response of FRP confined heat-damaged concrete columns based on the Assumption *iv*, which will be presented in the following section.

3- Determination of Information of Ultimate Point

3.1- Sub-model for Determining the Ultimate Stress (f_{cu}) at Ambient Conditions

Based on experimental observations, stress–strain curves of FRP confined concrete columns at room temperature can be generally classified into two categories as ascending (strain hardening) and descending (strain softening) type curves in the post transition phase of its axial response. In the former, the element ultimate compressive strength, f_{cu}, is higher than f_{ctr}. For specimens with an adequate FRP confinement, due to the noticeable ability of the confining system in restraining the concrete transverse expansion and volumetric response, there is an ascending branch in the stress-strain curve after the transition stage, therefore $E_2 > 0$. Regarding the second category, f_{cu} is lower than f_{ctr}, with a descending branch (strain softening) for $\varepsilon_c > \varepsilon_{ctr}$, therefore $E_2 < 0$. In such cases, due to the relatively low stiffness of the FRP confinement system, the confinement benefits affects the concrete response only in terms of post-peak load carrying capacity and energy absorption, with a significant concrete expansion at failure.

Based on the aforementioned discussion, since a sufficient level of the confinement is designed/prescribed apparently in real cases of axial strengthening, the focus of the current study was given on the case of sufficiently confined concrete, in the compliance with design purposes. Accordingly, the applicability of the proposed model is rationally limited to concrete columns sufficiently confined by FRP with an ascending type curve ($E_2 > 0$ and $f_{cu} > f_{ctr}$).

It is well-known that the level of axial strength enhancements (f_{cu}/f_{c0}) is strongly dependent on FRP confinement ($f_{l,rup}/f_{c0}$) imposed to the concrete corresponding to its ultimate axial strain (ε_{cu}) at FRP rupture strain ($\varepsilon_{f,rup}$). Accordingly, the axial strength model can be expressed as $f_{cu}/f_{c0} = 1 + B_0\left(f_{l,rup}/f_{c0}\right)^{B_1}$ where B_0 and B_1 are calibration factors. Considering $\varepsilon_{f,rup}$ is a percentage of the FRP ultimate tensile strain (ε_{fu}), in order to construct a proper structure for a regression analysis-based predictive model, the strength model was rearranged as follows:

$$\frac{f_{cu}}{f_{c0}} = 1 + B_0\left(\frac{f_{l,rup}}{f_{c0}}\right)^{B_1} \simeq 1 + B_2\left(K_L\right)^{B_3}\left(f_{c0}\right)^{B_4}\left(\varepsilon_{fu}\right)^{B_5} \qquad (K_L \text{ and } f_{c0} \text{ are in MPa}) \tag{13}$$

in which

$$K_L = 2\frac{n_f^k t_f E_f}{b} \qquad (E_f \text{ in MPa, and } t_f \text{ and } b \text{ in mm}) \tag{14}$$

where B_2, B_3, B_4 and B_5 are calibration factors; n_f is the number of FRP layers; t_f is the nominal thickness of a FRP layer; E_f is the FRP elasticity modulus; κ is equal to 1 and 0.85 corresponding to $n_f \le 3$ and $n_f \ge 4$, respectively, according to *fib* bulletin 90 recommendation [29]. Based to the best-fit results for the calibration factors obtained from regression analyses

performed on test data of FCCC/FCSC, presented in Appendix A, ($B_2 = 2.6/(\beta_{SE}\beta_R)$, $B_3 = 0.93$, $B_4 = -1.28$ and $B_5 = 0.69$), a new formulation is proposed to calculate f_{cu} by:

$$\frac{f_{cu}}{f_{c0}} = 1 + \frac{2.6}{\beta_{SE}\beta_R} K_L^{\,0.93} f_{c0}^{\,-1.28} \varepsilon_{fu}^{\,0.69} \tag{15}$$

in which

$$\beta_{SE} = \left(\frac{b}{150}\right)^{0.2} \leq 1.1 \tag{16}$$

$$\beta_R = 0.85\left(R_b\right)^{-0.75} \geq 1 \tag{17}$$

where β_{SE} and β_R represent the terms addressing the effects of column's cross section dimension and corner radius ratio ($R_b = 2r/b$, with $R_b = 1$ for circular cross-section) on the axial strength enhancements. In Fig. 4a and 4b, the performance of the developed model (Eq. (15)) for predicting the relevant experimental data of FCCC/FCSC specimens is, respectively, demonstrated. Based on the statistical indicators (*Mean Value* (MV), *Coefficient of Variation* (CoV), *Mean Absolute Percentage Error* (MAPE), and *R-squared* (R^2)), the proposed model is able to efficiently predict the experimental f_{cu} of both FCCC and FCSC, confirming the reliability of the calibration factors obtained from the statistical analysis.

3-2- Sub-model for Ultimate Stress ($f_{cu,T}$) at Elevated Conditions

Experimental evidence shows that increasing T_m, the peak strength of unconfined heat-damage concrete is reduced from f_{c0} at ambient conditions to f_{c0}^T at elevated temperature. Accordingly, the peak axial strength of FCHCC and FCHSC can be determined from Eq. (15) by substituting f_{c0} with f_{c0}^T as:

$$\frac{f_{cu,T}}{f_{c0}^{T}}=1+\frac{2.6}{\beta_{SE}\beta_{R}}\left(K_{L}\right)^{0.93}\left(f_{c0}^{T}\right)^{-1.28}\left(\varepsilon_{fu}\right)^{0.69} \quad (18)$$

A close look at Eq. (18) demonstrates that the effectiveness of FRP confining system on FCHCC/FCHSC is assumed the same of that of FCCC/FCSC with identical concrete strength. To highlight the effect of pre-existing thermal damage on the effectiveness of FRP confinement system, the ratio of confinement-induced enhancements obtained analytically over experimentally, defined by an error index Y_1 $\left(=\left(f_{cu,T}/f_{c0}^{T}-1\right)^{Ana}\Big/\left(f_{cu,T}/f_{c0}^{T}-1\right)^{Exp}\right)$ is evaluated in Fig. 5a. As can be seen, Eq. (18) results in substantial underestimations in terms of f_{cu} by increasing T_m imposed to concrete. It shows the necessity of considering the thermal damage influence on the effectiveness increase of the FRP confinement imposed to heat-damaged concrete. Accordingly, applying regression analysis to the experimental data of FCHCC/FCHSC (presented in Appendix A), the best-fit expression of Y_1 versus T_m relation was derived as $Y_1=0.59\left(T_m/1000\right)^{-0.1}\le 1$. By reflecting the influences of concrete strength (f_{c0}), corner radius ratio (R_b) and cooling regime (in water or air) in the developed Y_1 based on the experimental data, the following extra calibration factor is added to Eq. (18):

$$\beta_{T}=7.25\beta_{cm}\beta_{T0}\left(\frac{1.2-0.2R_{b}}{f_{c0}^{\,0.72}}\right)\left(\frac{T_m}{1000}\right)^{-0.1}\le 1 \quad (19)$$

in which

$$\beta_{T0}=2-5\left(\frac{T_m}{1000}\right)\le 1 \quad (20)$$

and β_{cm} is equal to 1 and 1.175 for air-cooling method and water-cooling method, respectively, obtained based on the experimental results reported by Lenwari *et al.* [5]. Hence, by

introducing β_T (Eq. (19)) reflecting the thermal damage influence on FRP confinement-induced improvements into Eq. (18), the peak axial strength of FCHCC and FCHSC ($f_{cu,T}$) can be calculated as:

$$\frac{f_{cu,T}}{f_{c0}^{T}} = 1 + \frac{2.6}{\beta_{SE}\beta_R\beta_T} K_L^{0.93} f_{c0}^{T-1.28} \varepsilon_{fu}^{0.69} \tag{21}$$

It should be noted that, for concrete at room temperature, β_T is equal to 1, therefore Eqs. (21) degenerates in Eq. (15), which represents the successful establishment of the exposure temperature unification in the strength model development. Fig. 5b compares the results obtained experimentally from Bisby *et al.* [4], Lenwari *et al.* [5], Ouyang *et al.* [6] and Song *et al.* [7] with those predicted by the proposed unified model. As can be seen, the model is able to predict closely the experimental data of FCHCC/FCHSC confirming its suitable predictive performance.

4-1- Sub-model for Ultimate Strain (ε_{cu}) at Ambient Conditions

Ultimate axial strain (ε_{cu}) of FCCC/FCSC occurs when hoop strain in FRP jacket reaches its tensile rupture strain, $\varepsilon_{h,rup}$. Considering Poisson's ratio effect, ε_{cu} can be expressed as the ratio of $\varepsilon_{h,rup}$ and ultimate secant Poisson's ratio (υ_u) as:

$$\frac{\varepsilon_{cu}}{\varepsilon_{c0}} = \frac{\varepsilon_{h,rup}}{\upsilon_u \varepsilon_{c0}} = \frac{\psi \varepsilon_{fu}}{\upsilon_u \varepsilon_{c0}} \tag{22}$$

where ψ is a constant value representing the ratio of $\varepsilon_{h,rup}$ and ε_{fu} (Teng *et al.* [19]). Since υ_u is a main function of confinement stiffness (K_L / f_{c0} based on Eq. (14)) as evidenced by [30-34], and also ε_{c0} is essentially dependent on f_{c0} ([35-37]), ε_{cu} in Eq. (22) is restructured to develop a regression-based predictive model:

$$\frac{\varepsilon_{cu}}{\varepsilon_{c0}} = C_0 K_L^{\,C_1} f_{c0}^{\,C_2} \varepsilon_{fu}^{\,C_3} \tag{23}$$

where C_0, C_1, C_2 and C_3 are calibration factors, equal to $C_0 = 300/\alpha_{SE}\alpha_R$, $C_1 = 0.56$, $C_2 = -0.78$ and $C_3 = 1.17$, obtained from the statistical analysis with experimental data of FCCC/FCSC (Appendix A), which gives

$$\frac{\varepsilon_{cu}}{\varepsilon_{c0}} = \frac{300}{\alpha_{SE}\alpha_R} K_L^{\,0.56} f_{c0}^{\,-0.78} \varepsilon_{fu}^{\,1.17} \tag{24}$$

in which

$$\alpha_{SE} = \left(\frac{b}{150}\right)^{0.12} \le 1 \tag{25}$$

$$\alpha_R = \left(2.2 - 7R_b\right)\frac{\mathrm{e}^{-170X_r}}{R_b^{\,0.2}} \ge \frac{\mathrm{e}^{-170X_r}}{R_b^{\,0.2}} \tag{26}$$

$$X_r = \left(1 - R_b\right)\varepsilon_{fu} / f_{c0} \tag{27}$$

where α_{SE} and α_R represent the terms addressing the effects of column's cross section dimension and corner radius ratio on the axial strength enhancements. In Fig. 6a and 6b, the predictive performance of the developed model (Eq. (24)) for predicting the experimental data registered on FCCC and FCSC specimens, respectively, is demonstrated. Based on the statistical indicators, the proposed model is able to efficiently predict the experimental ε_{cu} of both FCCC and FCSC, confirming the reliability of the calibration factors obtained from the statistical analysis.

4-2- Sub-model for Ultimate Strain ($\varepsilon_{cu,T}$) at Elevated Conditions

For the determination of the ultimate strain ($\varepsilon_{cu,T}$) of FCHCC/FCHSC, the approach already adopted for the ultimate stress of FCCC/FCSC at elevated conditions was taken, by replacing

the concrete characteristics at ambient conditions for those at heat-damaged conditions. Accordingly, based on Eq. (24), by substituting f_{c0} and ε_{c0} with f_{c0}^{T} and ε_{c0}^{T}, respectively, $\varepsilon_{cu,T}$ is derived as:

$$\frac{\varepsilon_{cu,T}}{\varepsilon_{c0}^{T}} = \frac{300}{\alpha_{SE}\alpha_{R}} \left(K_L\right)^{0.56} \left(f_{c0}^{T}\right)^{-0.78} \left(\varepsilon_{fu}\right)^{1.17} \tag{28}$$

By defining a reduction factor α_T considering an error index of Eq. (28) ($\alpha_T = \varepsilon_{cu,T}^{Ana} / \varepsilon_{cu,T}^{Exp}$), the predictive performance of Eq. (28) can be evaluated with respect to thermal damage level based on the existing experimental data. As can be seen in Fig. 7a, Eq. (28) overestimates remarkably the experimental counterparts ($\alpha_T \geq 1$), which highlights the necessity for considering a reduction factor in Eq. (28) to decrease the confinement-induced improvements with T_m in terms of $\varepsilon_{cu,T}$. Accordingly, based on regression analysis performed on 141 experimental data (Appendix A), the best-fit expression of α_T versus T_m relation was derived as a 3rd degree polynomial equation format (Fig. 7a):

$$\alpha_T = \alpha_{cm}\left[112\left(\frac{T_m}{1000}\right)^3 - 129\left(\frac{T_m}{1000}\right)^2 + 52\left(\frac{T_m}{1000}\right) - 4\right] \geq 1 \tag{29}$$

where α_{cm} is equal to 1 and 0.65 for air-cooling method and water-cooling method, respectively, obtained based on the experimental results reported by Lenwari *et al.* [5]. By introducing the parameter α_T, from Eq. (29), into Eq. (28), $\varepsilon_{cu,T}$ of FCHCC/FCHSC can be proposed as:

$$\frac{\varepsilon_{cu,T}}{\varepsilon_{c0}^{T}} = \frac{300}{\alpha_{SE}\alpha_{R}\alpha_{T}} K_L^{\,0.56} f_{c0}^{T\,-0.78} \varepsilon_{fu}^{\,1.17} \tag{30}$$

where the model has a unified character with the case of concrete at the room temperature (FCCC/FCSC with $\alpha_T = 1$). In Fig. 7b, the performance of the proposed model is assessed based on the experimental results reported by Bisby *et al.* [4], Lenwari *et al.* [5], Ouyang *et al.* [6] and Song *et al.* [7]. It shows that there is a good agreement between both the experimental and analytical data of FCHCC/FCHSC. As a result, by calculating $f_{cu,T}$ and its corresponding strain of $\varepsilon_{cu,T}$, by Eq. (21) and (30), respectively, their information can be addressed for the determination of stress-strain relation model.

5.1- Sub-models for Transition Point (ε_{ctr}, f_{ctr}) at Ambient Conditions

This section introduces the determination of the axial stress and its corresponding strain at the transition zone for FRP confined heat-damaged concrete columns. Lam and Teng [17] presented a formulation to calculate axial strain (ε_{ctr}) of FCCC at ambient condition as follows:

$$\frac{\varepsilon_{ctr}}{\varepsilon_{c0}} = \frac{2 f_{c0}}{\varepsilon_{c0}\left(E_c - \frac{f_{cu} - f_{c0}}{\varepsilon_{cu}} \right)} \tag{31}$$

This equation is a function of the dependent variables of ε_{c0} and E_c (both directly correlated to f_{c0}) and f_{cu} and ε_{cu} (directly correlated to K_L and f_{c0}), and the independent variable of f_{c0}. Accordingly, due to the relative complex format of Eq. (31), to reduce/simplify the dependent variables with the corresponding independent variable(s), a simplification can potentially improve its practicability. For this purpose, through Eq. (31), by assuming f_{cu} and ε_{cu} calculated by Eqs. (15, 24), and $E_c = 4730\sqrt{f_{c0}}$ [26], a series of data for ε_{ctr} was generated analytically. Based on a regression analysis performed on this dataset, Eq. (31) was simplified as a main function of f_{c0} and K_L:

$$\frac{\varepsilon_{ctr}}{\varepsilon_{c0}} \simeq 0.45 {f_{c0}}^{0.25} + 0.0075 {K_L}^{0.37} \geq 1 \quad (32)$$

where the reliability of the simplification can be found in Fig. 8. When ε_{ctr} is available from Eq. (32), its corresponding stress (f_{ctr}^{Exp}) can be extracted from experimental axial stress versus strain relation of FCCC/FCSC. Accordingly, in this study, a test dataset of f_{ctr}^{Exp} was collected from experimental studies available in the literature. Fig. 9a demonstrates the relationship of axial strength effectiveness ($\left[f_{ctr}^{Exp} / f_{c0} - 1 \right]$) at the transition point with respect to the normalized confinement stiffness variable, K_L / f_{c0}. As can be seen, there is a significant correlation between the axial strength effectiveness and K_L / f_{c0} where their best-fit relation was obtained from regression analysis as $\left[f_{ctr}^{Exp} / f_{c0} - 1 \right] = 0.029\sqrt{K_L / f_{c0}}$ having a good performance. Therefore, f_{ctr} as a function of K_L / f_{c0} can be expressed as:

$$\frac{f_{ctr}}{f_{c0}} = 1 + 0.029\sqrt{\frac{K_L}{f_{c0}}} \quad (33)$$

whose suitable reliability was demonstrated in Fig. 9b.

5.2- Sub-models for Transition Point ($\varepsilon_{ctr,T}$, $f_{ctr,T}$) at Elevated Conditions

For the case of heat-damaged concrete with FRP confinement, by adopting Eq. (32) developed for cases at room temperature, the axial strain ($\varepsilon_{ctr,T}$) corresponding to the transition zone can be calculated by:

$$\frac{\varepsilon_{ctr,T}}{\varepsilon_{c0}^{T}} = 0.45\left(f_{c0}^{T} \right)^{0.25} + 0.0075 {K_L}^{0.37} \geq 1 \quad (34)$$

Therefore, through calculating $\varepsilon_{ctr,T}$ by Eq. (34), the corresponding stress ($f_{ctr,T}^{Exp}$) can be found from experimental axial responses of FCHCC/FCHSC. Experimental observations (i.e. Bisby *et al.* [4]) have evidenced that by increasing the level of thermal damage (T_m), the difference between column axial stiffness at the transition zone ($E_{ctr} = f_{ctr,T}/\varepsilon_{ctr,T}$) and at the ultimate stage ($E_{cu} = f_{cu,T}/\varepsilon_{cu,T}$) decreases considerably (as illustrated in Fig. 10a). For FCHCC/FCHSC with severe thermal damage (around $T_m = 800\ ^{o}\mathrm{C}$), the column behaves almost linearly with a constant axial stiffness ($E_{ctr} \simeq E_2$). Therefore, by introducing ψ_T as the ratio of E_{ctr} and E_{cu} ($\psi_T = E_{ctr}/E_{cu}$), $f_{ctr,T}$ can be expressed as $f_{ctr,T} = \psi_T E_{cu} \varepsilon_{ctr,T}$. In Fig. 10b is represented the variation of ψ_T with T_m based on the test data extracted from the experiments conducted by [4-7]. It can be seen that ψ_T decreases with the increase of T_m. By performing regression analysis with the experimental results, it was obtained $\psi_T = 6.74\left[4.5 - 3.5\left(T_m/1000\right)\right]$ for the best fit relation. By considering other influential factors (K_L and R_b) in the regression analysis of ψ_T and T_m variables, a new expression was proposed for the calculation of $f_{ctr,T}$ as follows:

$$f_{ctr,T} = \psi_T \frac{f_{cu,T}\varepsilon_{ctr,T}}{\varepsilon_{cu,T}} \geq f_{c0}^{T}\left(1 + 0.029\sqrt{\frac{K_L}{f_{c0}^{T}}}\right) \leq f_{cu,T} \tag{35}$$

in which

$$\psi_T = \frac{\left(K_L\right)^{0.3}}{\psi_0\left(R_b\right)^{0.15}}\left[0.43 - 0.33\left(\frac{T_m}{1000}\right)\right] \tag{36}$$

$$\psi_0 = \left(\frac{200}{T_m}\right) \geq 1 \tag{37}$$

where for cases at room temperature, Eq. (35) gives the same results as Eq. (33) confirming its unified character. Fig. 10c shows the performance of Eq. (35) against the experimental results ([4-7]). As can be seen, the developed model is able to provide accurate predictions of the counterpart data, representing its reliability. As a result, by calculating $f_{ctr,T}$, $\varepsilon_{ctr,T}$, $f_{cu,T}$ and $\varepsilon_{cu,T}$ using Eqs. (35, 34, 21, 30), the information of the key components of the proposed stress-strain model can be addressed.

6- Verification of the Proposed Design-oriented Model

In this section, the verification of the DOM developed in the present study to predict the axial stress versus axial strain relationship of FRP fully confined heat-damaged concrete is demonstrated. For this purpose, experimental stress-strain data are compared to those obtained analytically from the proposed DOM. For a further assessment of the developed stress-strain model (Eq. (10)), the well-established model developed by Teng *et al.* [17] (suggested exclusively for cases at room temperature) was generalized for FRP fully confined concrete with pre-existing thermal damage. In this model, ultimate stress and strain values were calculated based on the well-calibrated models proposed in this study (Eqs. (21) and (30)). The details of the generalized Teng *et al.* [17]'s model can be found in Appendix B.

The calculation process of the proposed DOM to obtain the axial stress versus strain relationships of heat-damaged/unheated concrete confined by FRP is based on the following steps:

i) Calculate the axial strain at the ultimate stage ($\varepsilon_{cu,T}$) using Eq. (30)

ii) Calculate the axial stress at the ultimate stage ($f_{cu,T}$) using Eq. (21)

iii) Calculate the axial strain at the transition zone ($\varepsilon_{ctr,T}$) using Eq. (34)

iv) Calculate the axial stress at the transition zone ($f_{ctr,T}$) using Eq. (35)

v) Assume a level of axial strain (ε_c)

vi) Calculate the corresponding axial stress (f_c) using Eq. (10)

vii) Draw f_c versus ε_c relationship

In the present study, the well-calibrated models developed by Shayanfar *et al.* [28] was followed to calculate the mechanical characteristics of unconfined heat-damaged concrete columns (f_{c0}^T and ε_{c0}^T), as presented in Appendix C. Furthermore, to calculate axial strain (ε_{c0}) corresponding to f_{c0}, the well-calibrated formulation recommended by Shayanfar *et al.* [36] was adopted as $\varepsilon_{c0} = 0.0011\left(f_{c0} L/b \right)^{0.25}$ where L is the height of the specimens.

Fig. 11 compares analytical simulations obtained from the proposed model and the generalized Teng *et al.* [17]'s model with FCCC/FCHCC measured experimentally by [4-6, 38, 39]. As can be seen, by using the generalized Teng *et al.* [17]'s stress-strain base model, despite accurate agreement between analytical and experimental results for FCCC, misleading predictions are obtained, particularly for FCCC with severe thermal-induced damage. However, the proposed DOM is able to predict the experimental counterparts of FCCC/FCHCC with the various levels of pre-existing thermal-induced damage with a good precision.

In Fig. 12, the performances of the proposed DOM and the generalized Teng *et al.* [17]'s model are compared in the simulation of experimental data of FCSC/FCHSC conducted by [7, 12]. It can be seen that the proposed DOM reveals much better predictions of stress-strain relation for square cross-section specimens compared to the generalized Teng *et al.* [17]'s model.

Based on the predictions results obtained not only for complete stress-strain relations shown in Figs. 11 and 12, but also for its critical coordinates at the transition an ultimate stages as presented in Figs. 5, 7 and 10, the reliability of the proposed DOM for FCHCC/ FCHSC can be confirmed.

7- Limitations of the Proposed Model

The proposed model was built using regression analysis technique performed on a set of experimental information obtained from small prototypes submitted to high temperature (FCHCC/FCHSC). Furthermore, the number of experimental tests in these conditions, is considerably smaller than of FCCC/FCSC at ambient (Appendix A). The database corresponding to the last ones type tests covers a wide-range of key variables of the geometry and the properties of concrete and FRP materials, which is not yet the case of FCHCC/FCHSC specimens. Accordingly, once a larger dataset with relevant test results of real scale FCHCC/FCHSC is available, the key components of the model can be recalibrated/updated, which also justifies making a continuous process of the data gathering and the model recalibration.

It is noteworthy that since the key components of the proposed model were calibrated based on the collected database of FCHCC/FCHSC (Appendix A), the proposed model is applicable to a wide range of the maximum exposure temperature as 200 °C to 800 °C, representing slight to severe thermal-damage levels, with a exposure duration in heating schemes in the range of two to three hours. Accordingly, for FCHCC/FCHSC submitted to a different heating scheme from those supported by the collected database (exposure temperature and exposure duration), a further verification and modification of the proposed model is required.

FRP confinement-induced improvements on the behavior of heat-damaged unreinforced concrete differ from those generated by dual confinement of FRP jacket and existing steel stirrups/hoops in heat-damaged RC columns. Furthermore, for the case of heat-damaged RC columns, there would be a certain level of degradations in longitudinal and transverse reinforcements as well as their bond conditions to the heat-damaged concrete. Hence, several

modifications on the present model must be implemented to make it applicable to heat-damaged RC columns with a combined FRP jacket and steel stirrups/hoops.

Considering the fact that thermal-induced degradation in concrete proceeds from the lagging deep into the cross-section, the beneficial influence of FRP confinement strategy tends to reduce for larger cross-sections. The degree of the dominance of this phenomenon can be evaluated once adequate data from different cross-sectional dimensions could be available, which is still lacking in the literature. Therefore, the validation of the proposed model for FRP confined heat-damaged concrete columns with larger cross-sectional dimensions requires demonstration.

Furthermore, since the methodology presented in this work has a general nature, the developed model can be potentially extended for partially FRP confined concrete columns with rectangular cross-section, where the substantial influences of cross-sectional aspect ratio and partially imposed confinement system on stress-strain relationship need to be identified/considered. Further investigations in this area are suggested for future research studies.

8- Summary and Conclusions

This paper proposed a new generalized design-oriented (DOM) model to analytically calculate the axial response of FRP confined heat-damaged circular/square concrete columns (FCHCC/FCHSC). Based on experimental observation of axial stress-strain curves of FCHCC/FCHSC specimens, a closed-form formulation including parabolic and linear functions was developed which integrates a set of strength and strain sub-models to calculate the stress/strain information at the transition and ultimate points. To have a unified model for concrete at the room and elevated temperature conditions, initially, predictive formulations calculating stress/strain information at the transition and ultimate stages were developed based

on large test database with 1517 FCCC and 256 FCSC specimens at the ambient. Then, by applying them on 109 FCHCC and 35 FCHSC test specimens, the substantial influence of thermal-induced damages on these key stages was investigated, and reflected empirically in the model establishment as a function of the level of maximum temperature (T_m) exposed to the concrete. The proposed DOM model demonstrated an appropriate performance in the simulation of axial stress-strain of FCHCC/FCHSC, compared to existing modelling solutions. It should be noted that the proposed DOM does not represent a ready-to-use based predictive model for direct application in practice where safety factors obtained on the basis of Reliability Analysis as well as model recalibration based on a larger dataset consisting of relevant test results of real scale FCHCC/FCHSC are required.

Acknowledgments

This study is a part of the project ‘‘Sticker –Innovative technique for the structural strengthening based on using CFRP laminates with multifunctional attributes and applied with advanced cement adhesives’’, with the reference POCI-01-0247-FEDER-039755. The first author also acknowledges the support provided by FCT PhD individual fellowship 2019 with the reference of “SFRH/BD/148002/2019”.

Data Availability Statement

All data, models, and code generated or used during the study appear in the submitted article.

References

1- Kodur, V. (2014). Properties of concrete at elevated temperatures. International Scholarly Research Notices.

2- Bamonte, P., & Monte, F. L. (2015). Reinforced concrete columns exposed to standard fire: Comparison among different constitutive models for concrete at high temperature. Fire safety journal, 71, 310-323.

3- Demir, U., Green, M. F., & Ilki, A. (2020). Postfire seismic performance of reinforced precast concrete columns. PCI Journal, 65(6).

4- Bisby, L. A., Chen, J. F., Li, S. Q., Stratford, T. J., Cueva, N., & Crossling, K. (2011). Strengthening fire-damaged concrete by confinement with fibre-reinforced polymer wraps. Engineering Structures, 33(12), 3381-3391.

5- Lenwari, A., Rungamornrat, J., & Woonprasert, S. (2016). Axial compression behavior of fire-damaged concrete cylinders confined with CFRP sheets. Journal of Composites for Construction, 20(5), 04016027.

6- Ouyang, L. J., Chai, M. X., Song, J., Hu, L. L., & Gao, W. Y. (2021). Repair of thermally damaged concrete cylinders with basalt fiber-reinforced polymer jackets. Journal of Building Engineering, 44, 102673.

7- Song, J., Gao, W. Y., Ouyang, L. J., Zeng, J. J., Yang, J., & Liu, W. D. (2021). Compressive behavior of heat-damaged square concrete prisms confined with basalt fiber-reinforced polymer jackets. Engineering Structures, 242, 112504.

8- Elhamnike, S. M., Abbaszadeh, R., Razavinasab, V., & Ziaadiny, H. (2022). Behavior and modeling of post-heated circular concrete specimens repaired with fiber-reinforced polymer composites. Advances in Structural Engineering, 25(3), 541-551.

9- Eid, R., Roy, N., & Paultre, P. (2009). Normal-and high-strength concrete circular elements wrapped with FRP composites. Journal of composites for construction, 13(2), 113-124.

10- Barros JA, Ferreira DR. Assessing the efficiency of CFRP discrete confinement systems for concrete cylinders. J Compos Constr 2008;12(2):134-148.

11- Wu YF, Wei YY. Effect of cross-sectional aspect ratio on the strength of CFRP-confined rectangular concrete columns. Eng Struct 2010;32(1):32-45.

12- Shan B, Gui FC, Monti G, Xiao Y (2019). Effectiveness of CFRP confinement and compressive strength of square concrete columns. J Compos Constr 2019 23(6):04019043.

13- Teng J, Huang YL, Lam L, Ye LP. Theoretical model for fiber-reinforced polymer-confined concrete. J Compos Constr 2007;11(2):201-210.

14- Lim JC, Ozbakkaloglu T (2014a). Unified stress-strain model for FRP and actively confined normal strength and high-strength concrete. J Compos Constr 2014;19(4):04014072.

15- Shayanfar, J., Barros, J. A., & Rezazadeh, M. (2021). Generalized Analysis-oriented model of FRP confined concrete circular columns. Composite Structures, 270, 114026.

16- Shayanfar, J., Barros, J. A., & Rezazadeh, M. (2022). Unified model for fully and partially FRP confined circular and square concrete columns subjected to axial compression. Engineering Structures, 251, 113355.

17- Lam, L., and Teng, J. G. (2003). "Design-oriented stress-strain model for FRP-confined concrete." Constr. Build. Mater., 17(6), 471–489.

18- Lam, L., & Teng, J. G. (2003). Design-oriented stress-strain model for FRP-confined concrete in rectangular columns. Journal of reinforced plastics and composites, 22(13), 1149-1186.

19- Teng, J. G., Jiang, T., Lam, L., & Luo, Y. Z. (2009). Refinement of a design-oriented stress-strain model for FRP-confined concrete. Journal of Composites for Construction, 13(4), 269.

20- Wei, Y. Y., & Wu, Y. F. (2012). Unified stress–strain model of concrete for FRP-confined columns. Construction and Building Materials, 26(1), 381-392.

21- Fallahpour, A., Ozbakkaloglu, T., & Vincent, T. (2018). Simplified design-oriented axial stress-strain model for FRP-confined normal-and high-strength concrete. Engineering Structures, 175, 501-516.

22- Mander, J. B., Priestley, M. J., & Park, R. (1988). Theoretical stress-strain model for confined concrete. Journal of structural engineering, 114(8), 1804-1826.

23- Shayanfar, J., Barros, J. A., & Rezazadeh, M. (2022). Cross- sectional and confining system unification on peak compressive strength of FRP confined concrete. Structural Concrete.

24- Cao, Y. G., Jiang, C., & Wu, Y. F. (2016). Cross-sectional unification on the stress-strain model of concrete subjected to high passive confinement by fiber-reinforced polymer. Polymers, 8(5), 186.

25- Shayanfar, J., Kafshgarkolaei, H. J., Barros, J. A., & Rezazadeh, M. (2022). Unified Strength Model for FRP Confined Heat-damaged Circular and Square Concrete Columns. Composite Structures, 116647.

26- ACI. Guide for the design and construction of externally bonded FRP systems for strengthening concrete structures, ACI 440.2R-08. Farmington Hills (MI, USA): American Concrete Institute; 2008.

27- Ozbakkaloglu, T., & Lim, J. C. (2013). Axial compressive behavior of FRP-confined concrete: Experimental test database and a new design-oriented model. Composites Part B: Engineering, 55, 607-634.

28- Shayanfar, J., Barros, J. A., & Rezazadeh, M. (2023). Stress–strain model for FRP confined heat-damaged concrete columns. Fire Safety Journal, 136, 103748.

29- Fib Bulletin 90. Externally applied FRP reinforcement for concrete structures. Task Group 5. 1, International Federation for Structural Concrete 2019.

30- Baji, H., Ronagh, H. R., & Li, C. Q. (2016). Probabilistic design models for ultimate strength and strain of FRP-confined concrete. Journal of Composites for Construction, 20(6), 04016051.

31- Shayanfar, J., Rezazadeh, M., & Barros, J. A. (2020). Analytical model to predict dilation behavior of FRP confined circular concrete columns subjected to axial compressive loading. Journal of Composites for Construction, 24(6), 04020071.

32- Shayanfar, J., Rezazadeh, M., Barros, J., & Ramezansefat, H. (2020). A new dilation model for FRP fully/partially confined concrete column under axial loading. In RILEM Spring Convention and Conference (pp. 435-446). Springer, Cham.

33- Shayanfar, J., Rezazadeh, M., & Barros, J. A. (2022). Theoretical prediction of axial response of FRP fully/partially confined circular concrete under axial loading. In International Conference on Fibre-Reinforced Polymer (FRP) Composites in Civil Engineering (pp. 1439-1449). Springer, Cham.

34- Nematzadeh, M., Mousavimehr, M., Shayanfar, J., & Omidalizadeh, M. (2021). Eccentric compressive behavior of steel fiber-reinforced RC columns strengthened with CFRP wraps: Experimental investigation and analytical modeling. Engineering Structures, 226, 111389.

35- Yang, K. H., Lee, Y., & Mun, J. H. (2019). A Stress-Strain Model for Unconfined Concrete in Compression considering the Size Effect. Advances in Materials Science and Engineering, 2019.

36- Shayanfar, J., Barros, J. A., & Rezazadeh, M. (2023). Analysis-oriented model for partially FRP-and-steel-confined circular RC columns under compression. Engineering Structures, 276, 115330.

37- Shayanfar, J., Bengar, H. A., & Parvin, A. (2018). Analytical prediction of seismic behavior of RC joints and columns under varying axial load. Engineering Structures, 174, 792-813.

38- Lim, J. C., & Ozbakkaloglu, T. (2015). Hoop strains in FRP-confined concrete columns: experimental observations. Materials and Structures, 48(9), 2839-2854.

39- Zeng JJ, Guo YC, Gao WY, Chen WP, Li LJ. Stress-strain behavior of concrete in circular concrete columns partially wrapped with FRP strips. Compos Struct 2018;200:810-828.

40- Chang, Y. F., Chen, Y. H., Sheu, M. S., & Yao, G. C. (2006). Residual stress–strain relationship for concrete after exposure to high temperatures. Cement and concrete research, 36(10), 1999-2005.

Appendix A

See Table A1 to A6.

Appendix B

Lam and Teng [17] have developed a design-oriented model to determine axial stress versus axial strain curves of FRP confined concrete columns at room temperature. In the present paper, this model was generalized for cases with pre-existing thermal damage where their ultimate stress and strain values are calculated based on the well-calibrated models proposed in this study (Eqs. (21, 30)). Accordingly, at a given axial strain (ε_c), the corresponding axial stress (f_c) can be determined using the generalized Lam and Teng [17]'s model as:

$$f_c = E_c^T \varepsilon_c - \frac{\left(E_c^T - E_2\right)^2}{4 f_{c0}^T} \varepsilon_c^2 \qquad \text{for } \varepsilon_c \le \varepsilon_{ctr,T} \tag{B-1}$$

$$f_c = f_{c0} + E_2 \varepsilon_c \qquad \text{for } \varepsilon_c \ge \varepsilon_{ctr,T} \tag{B-2}$$

in which

$$\varepsilon_{ctr,T} = \frac{2 f_{c0}^T}{E_c^T - E_2} \tag{B-3}$$

$$E_2 = \frac{f_{cu,T} - f_{c0}}{\varepsilon_{cu,T}} \tag{B-4}$$

where E_c^T is the elastic modulus of heat-damaged concrete, which was determined by following Chang *et al.* [40]'s recommendation.

$$E_c^T = \left(1.033 - 0.00165T_m\right) E_c \qquad \text{for } T_m \le 125\ ^\circ\text{C} \tag{B-5}$$

$$E_c^T = \frac{E_c}{1.2 + 18\left(0.0015T_m\right)^{4.5}} \qquad \text{for } 125\ ^\circ\text{C} \le T_m \le 800\ ^\circ\text{C} \tag{B-6}$$

Appendix C

In the present study, to calculate the mechanical characteristics of unconfined heat-damaged concrete columns (f_{c0}^T and ε_{c0}^T), the models developed by Shayanfar *et al.* [28], calibrated based on a large test database, was followed. For the calculation of f_{c0}^T, the following equation of Eq. (C-1) was proposed as:

$$f_{c0}^T = \left(1.087 - 0.00116T_m\right)\frac{f_{c0}}{\gamma_f} \le f_{c0} \tag{C-1}$$

in which

$$\gamma_f = 1 + \left(\gamma_0 - 1\right)\left(\frac{T_m - 25}{100}\right) \qquad \text{for } T_m \le 100\ ^\circ\text{C} \tag{C-2a}$$

$$\gamma_f = \gamma_0 \qquad \text{for } T_m \ge 100\ ^\circ\text{C} \tag{C-2b}$$

$$\gamma_0 = 3415\left(\frac{f_{c0}}{1000}\right)^3 - 721\left(\frac{f_{c0}}{1000}\right)^2 + 44.5\left(\frac{f_{c0}}{1000}\right) + 0.178 \tag{C-3}$$

where γ_f is the calibration factor reflecting the effect of concrete strength on the magnitude of the decrease of f_{c0}^T with respect of T_m. Based on Shayanfar *et al.* [28]'s recommendation, ε_{c0}^T as a function of ε_{c0} $(= 0.0011\left(f_{c0}L/b\right)^{0.25}$ [36]) can be calculated as:

$$\varepsilon_{c0}^{T}=\left(1+63 f_{c0}{}^{-0.5}\left(\frac{T_m}{1000}\right)^{4.2}\right)\frac{\varepsilon_{c0}}{\alpha_{T0}}\le 4.5\frac{\varepsilon_{c0}}{\alpha_{T0}} \quad \text{(C-4)}$$

in which

$$\alpha_{T0}=1 \qquad \text{for } T_m\le 100\ ^{\circ}\text{C} \quad \text{(C-5a)}$$

$$\alpha_{T0}=1.22-0.0025T_m+3\times10^{-6}T_m{}^{2} \qquad \text{for } T_m>100\ ^{\circ}\text{C} \quad \text{(C-5b)}$$

where α_{T0} presents the calibration factor reflecting the influence of T_m on axial strain enhancement caused by thermal damage.

Figure 1

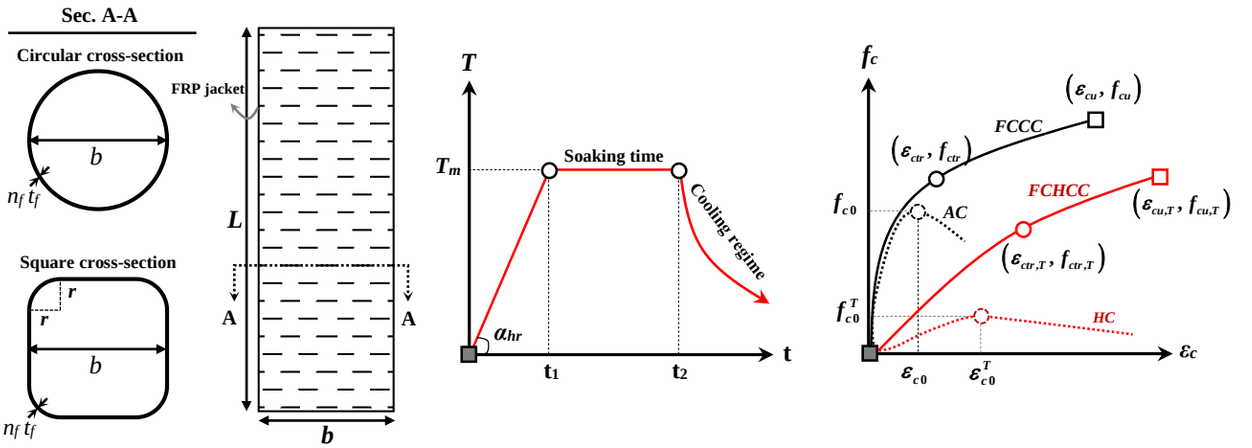

Fig. 1. a) Details of circular/square concrete columns with FRP full confinement; b) Typical temperature (T) versus time (t) curve as heating scheme; c) Typical axial stress (f_c) versus axial strain (ε_c) curve

Note: T_m = maximum exposure temperature (target temperature); α_{hr} = heating rate; t_1 = time at which the temperature (T) reaches T_m; t_2 = time at which the heating process terminates; f_{c0} = peak compressive stress of unconfined concrete columns at ambient conditions (AC); f_{c0}^T = peak compressive stress of unconfined heat-damaged concrete columns (HC); ε_{c0} = axial strain corresponding to f_{c0}; ε_{c0}^T = axial strain corresponding to f_{c0}^T; L = column's height; b = section dimension; r = corner radius; n_f = number of FRP layers; t_f = nominal FRP thickness.

Figure 2

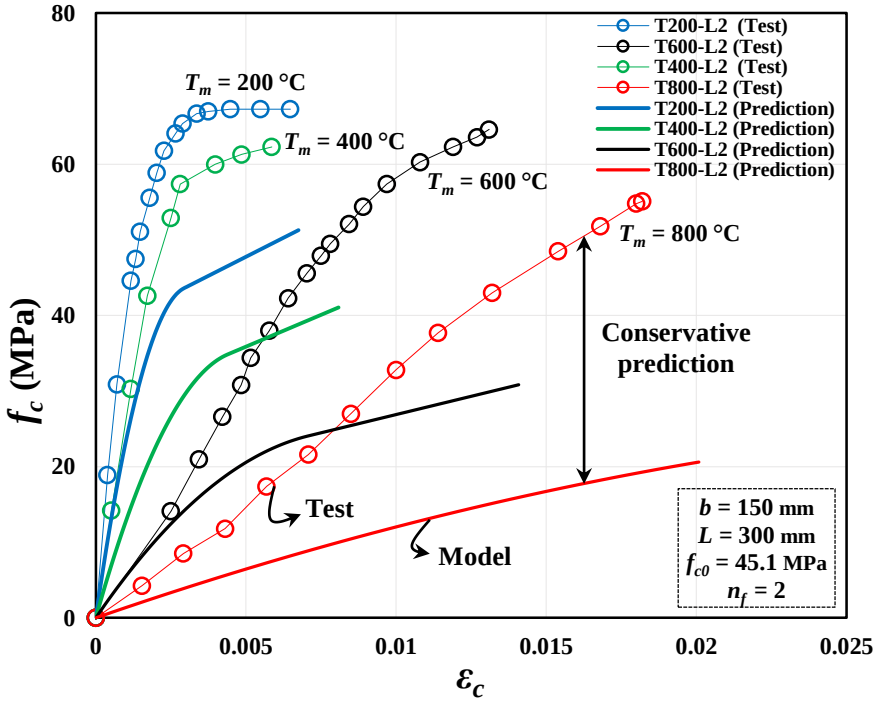

Fig. 2. Predictions from the generalized ACI 440.2R-08 [26]'s model versus test data for FCCC specimens tested by Ouyang *et al.* [6]

Figure 4

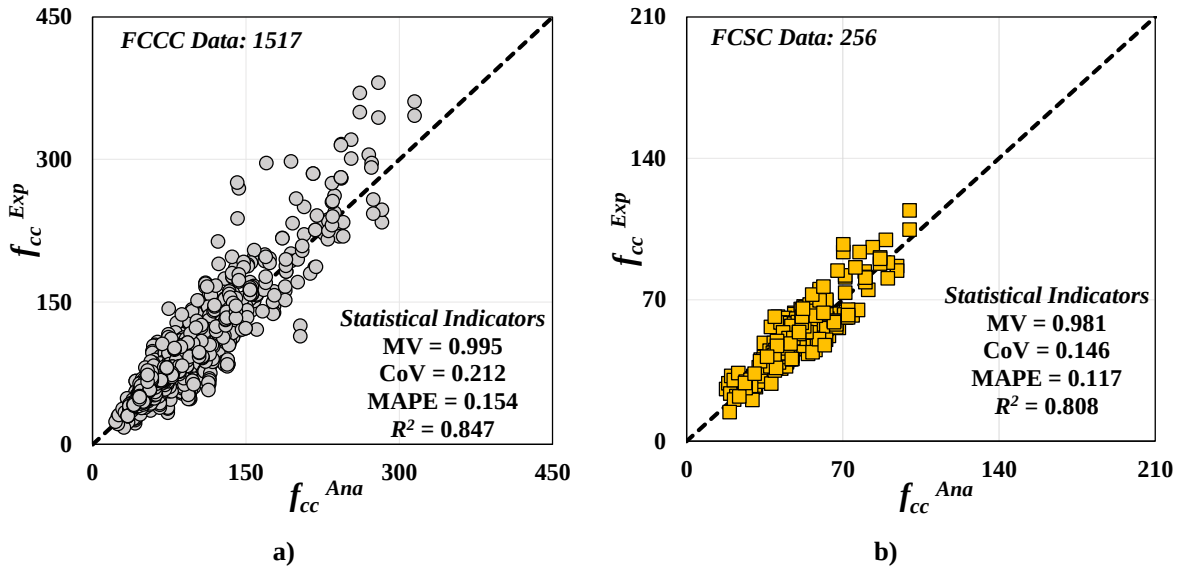

Fig. 4. Predictive performance of Eq. (15) for a) FCCC; b) FCSC

Figure 6

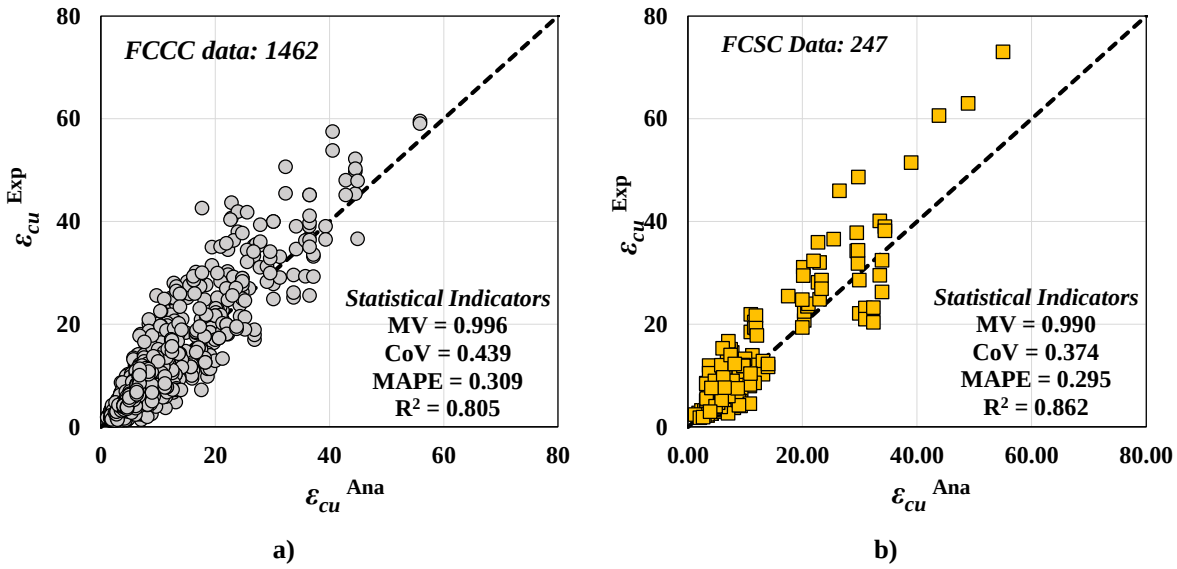

Fig. 6. Predictive performance of Eq. (24) for a) FCCC; b) FCSC

Figure 10

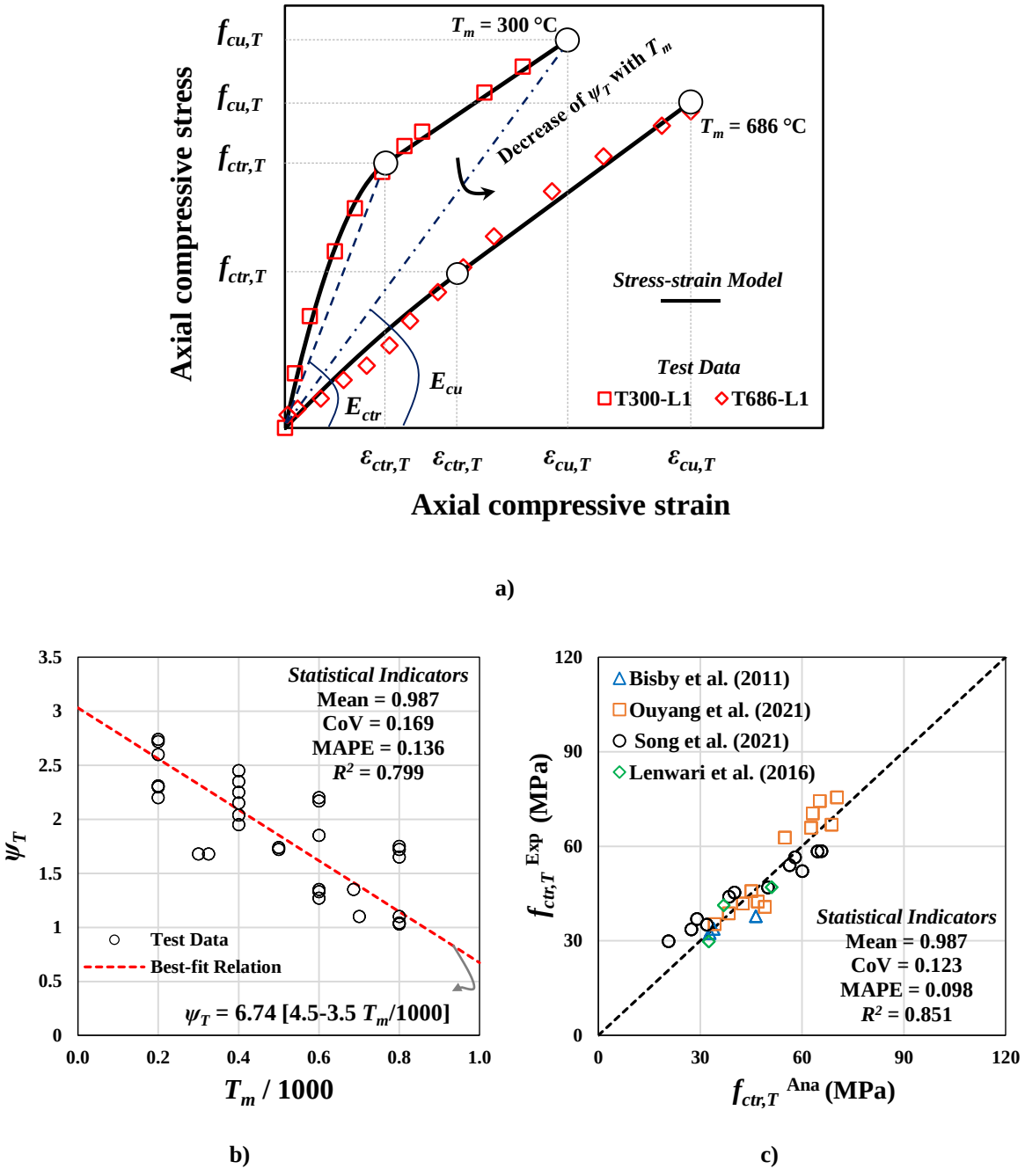

Fig. 10. a) Typical axial behavior of FRP confined heat-damaged concrete; b) Relation of ψ_T with T_m; c) Predictive performance of Eq. (35)

Figure 11

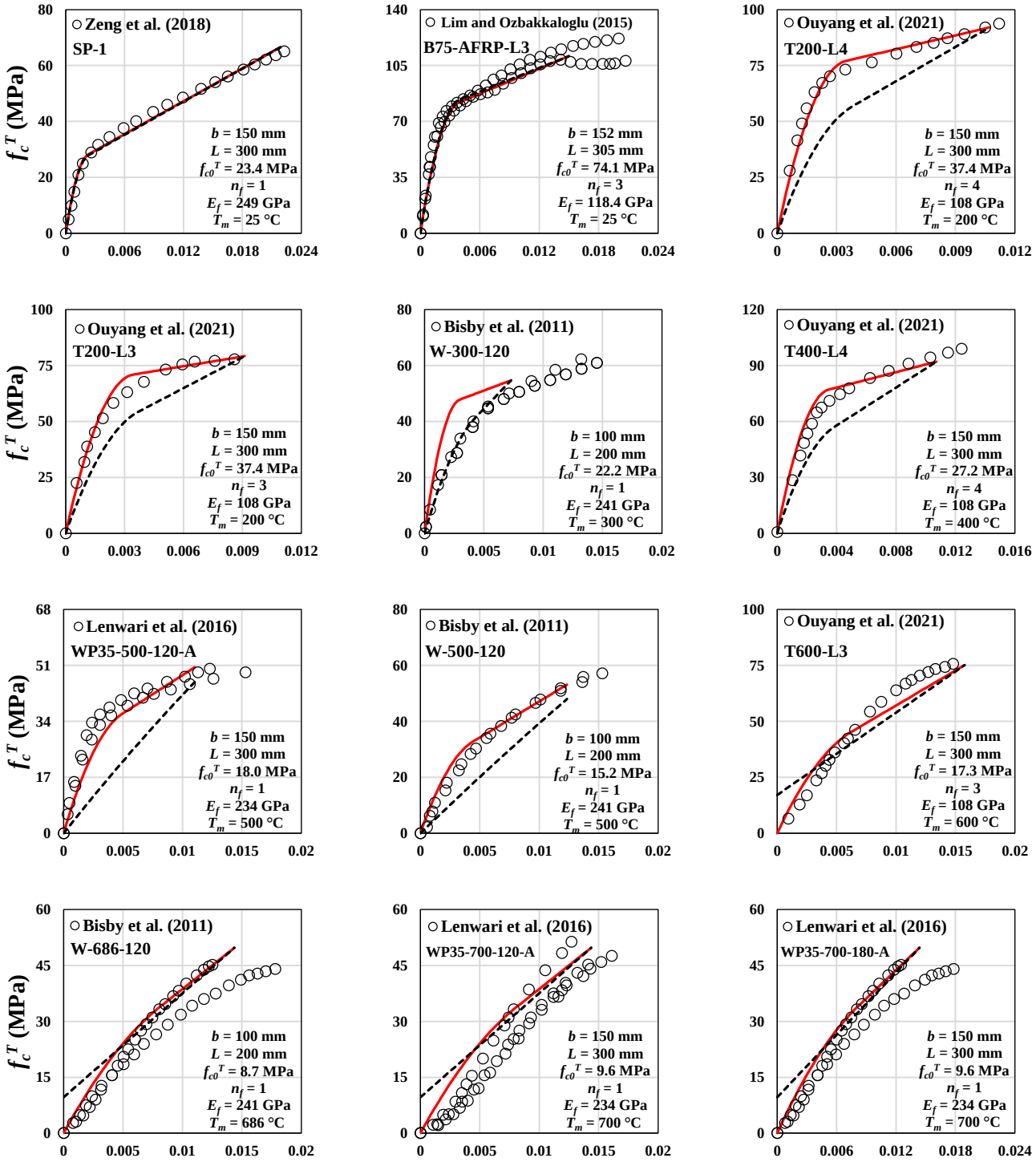

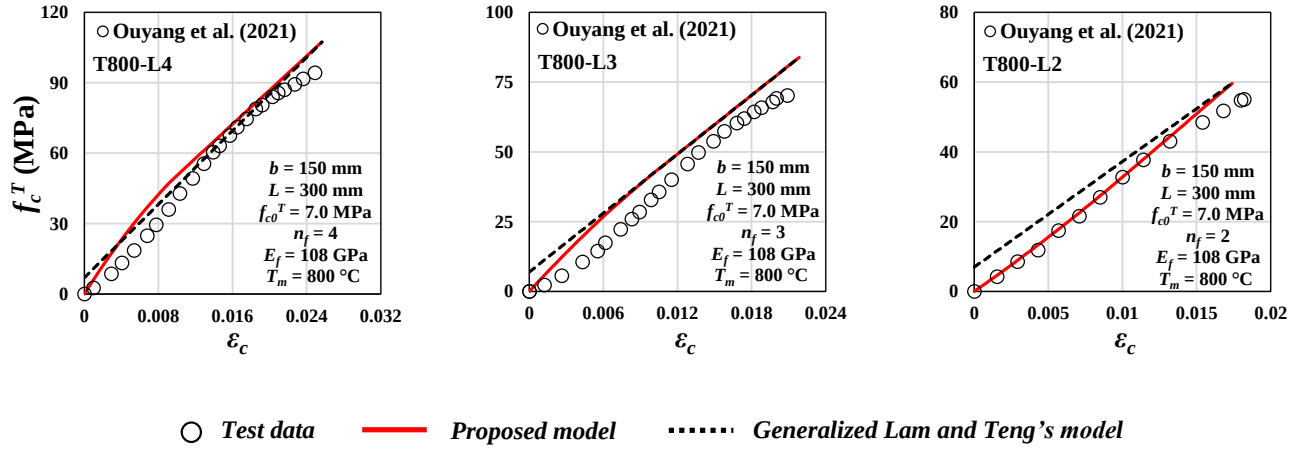

Fig. 11. Anaytical simulations against experimental data of FCCC/FCHCC

Figure 12

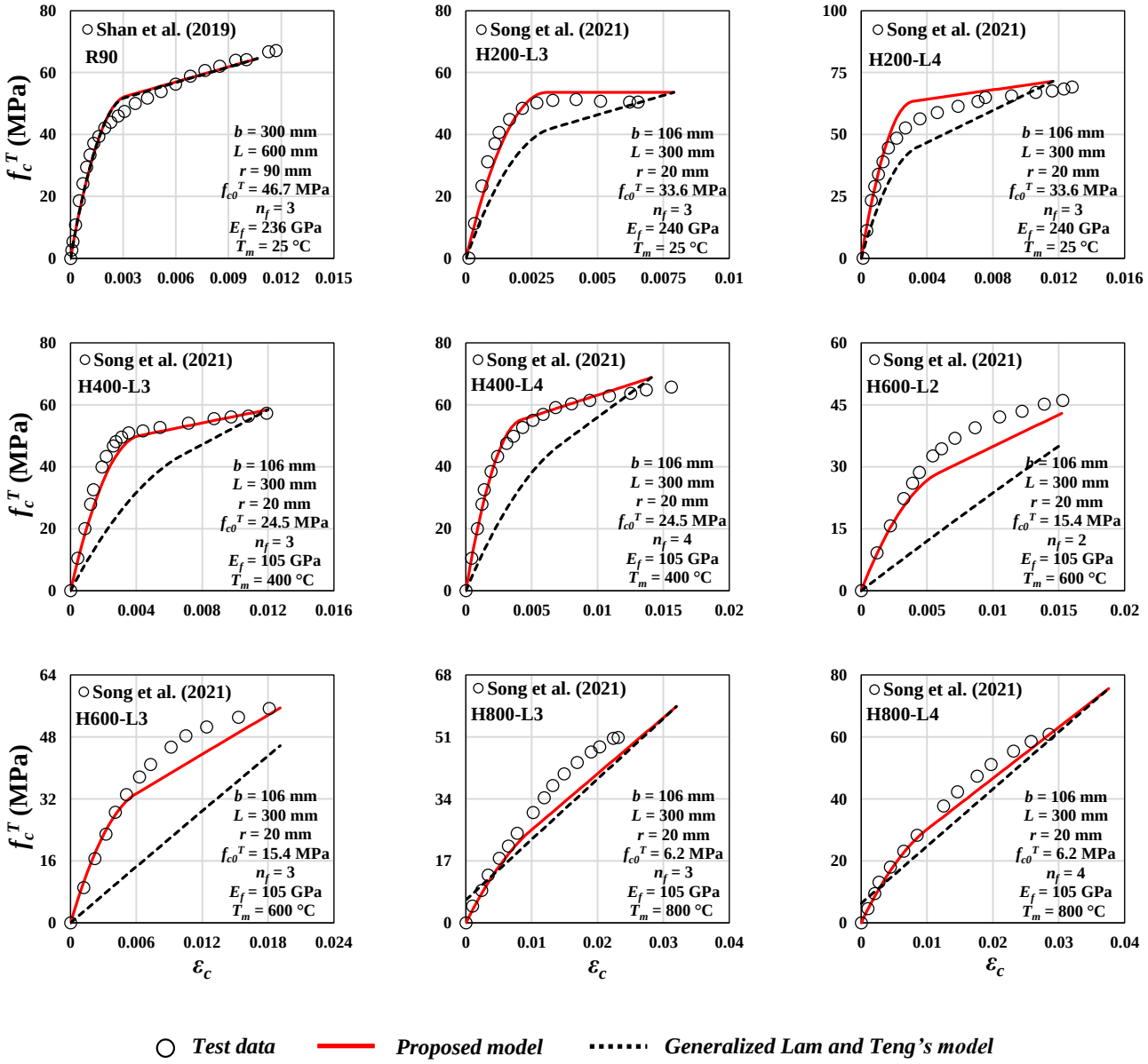

Fig. 11. Anaytical simulations against experimental data of FCSC/FCHSC

Table 1

Table. 1. Comparison of experimental and obtained results of β_T and $f_{cu,T}$

	Test ID	b (mm)	r (mm)	T (°C)	f_{c0} (MPa)	f_{c0}^{T} (MPa)	K_L (MPa)	β_T^{Exp}	β_T^{Ana}	β_T^{Exp} / β_T^{Ana}	$f_{cu,T}^{Exp}$ (MPa)	$f_{cu,T}^{Ana}$ (MPa)	$f_{cu,T}^{Exp}$ / $f_{cu,T}^{Ana}$
Ouyang *et al.* [6]	T200-L2-1	150	75	200	45.1	37.4	349	0.71	0.55	0.77	59	66	0.77
	T200-L2-2	150	75	200	45.1	37.4	349	0.53	0.55	1.04	67	66	1.04
	T200-L2-3	150	75	200	45.1	37.4	349	0.53	0.55	1.04	67	66	1.04
	T200-L3-1	150	75	200	45.1	37.4	524	0.56	0.55	0.98	78	79	0.98
	T200-L3-2	150	75	200	45.1	37.4	524	0.61	0.55	0.91	75	79	0.91
	T200-L3-3	150	75	200	45.1	37.4	524	0.57	0.55	0.97	78	79	0.97
	T200-L4-1	150	75	200	45.1	37.4	568	0.43	0.55	1.28	95	82	1.28
	T200-L4-2	150	75	200	45.1	37.4	568	0.41	0.55	1.33	97	82	1.33
	T200-L4-3	150	75	200	45.1	37.4	568	0.45	0.55	1.23	92	82	1.23
	T400-L2-1	150	75	400	45.1	27.2	349	0.50	0.51	1.02	61	61	1.02
	T400-L2-2	150	75	400	45.1	27.2	349	0.53	0.51	0.96	59	61	0.96
	T400-L2-3	150	75	400	45.1	27.2	349	0.49	0.51	1.05	62	61	1.05
	T400-L3-1	150	75	400	45.1	27.2	524	0.58	0.51	0.88	70	76	0.88
	T400-L3-2	150	75	400	45.1	27.2	524	0.48	0.51	1.06	79	76	1.06
	T400-L3-3	150	75	400	45.1	27.2	524	0.50	0.51	1.02	77	76	1.02
	T400-L4-1	150	75	400	45.1	27.2	568	0.34	0.51	1.52	107	80	1.52
	T400-L4-2	150	75	400	45.1	27.2	568	0.36	0.51	1.41	101	80	1.41
	T400-L4-3	150	75	400	45.1	27.2	568	0.37	0.51	1.38	100	80	1.38
	T600-L2-1	150	75	600	45.1	17.1	349	0.49	0.49	1.00	57	57	1.00
	T600-L2-2	150	75	600	45.1	17.1	349	0.38	0.49	1.28	68	57	1.28
	T600-L2-3	150	75	600	45.1	17.1	349	0.41	0.49	1.19	64	57	1.19
	T600-L3-1	150	75	600	45.1	17.1	524	0.44	0.49	1.11	81	75	1.11
	T600-L3-2	150	75	600	45.1	17.1	524	0.50	0.49	0.99	74	75	0.99
	T600-L3-3	150	75	600	45.1	17.1	524	0.48	0.49	1.02	76	75	1.02
	T600-L4-1	150	75	600	45.1	17.1	568	0.41	0.49	1.21	92	79	1.21
	T600-L4-2	150	75	600	45.1	17.1	568	0.38	0.49	1.30	98	79	1.30
	T600-L4-3	150	75	600	45.1	17.1	568	0.41	0.49	1.20	92	79	1.20
	T800-L2-1	150	75	800	45.1	7.0	349	0.48	0.48	0.99	59	59	0.99
	T800-L2-2	150	75	800	45.1	7.0	349	0.49	0.48	0.98	58	59	0.98
	T800-L2-3	150	75	800	45.1	7.0	349	0.51	0.48	0.93	56	59	0.93
	T800-L3-1	150	75	800	45.1	7.0	524	0.56	0.48	0.85	72	83	0.85
	T800-L3-2	150	75	800	45.1	7.0	524	0.55	0.48	0.86	73	83	0.86
	T800-L3-3	150	75	800	45.1	7.0	524	0.58	0.48	0.83	70	83	0.83
	T800-L4-1	150	75	800	45.1	7.0	568	0.47	0.48	1.01	90	89	1.01
	T800-L4-2	150	75	800	45.1	7.0	568	0.47	0.48	1.01	90	89	1.01
	T800-L4-3	150	75	800	45.1	7.0	568	0.45	0.48	1.05	93	89	1.05
Song *et al.* [7]	H200L2-A	106	20	200	40.2	33.6	479	0.77	0.67	0.88	51	53	0.88
	H200L2-B	106	20	200	40.2	33.6	479	0.77	0.67	0.87	51	53	0.87
	H200L2-C	106	20	200	40.2	33.6	479	0.78	0.67	0.86	50	53	0.86
	H200L3-A	106	20	200	40.2	33.6	719	1.03	0.67	0.65	52	62	0.65
	H200L3-B	106	20	200	40.2	33.6	719	0.78	0.67	0.86	58	62	0.86
	H200L3-C	106	20	200	40.2	33.6	719	0.80	0.67	0.84	58	62	0.84
	H200L4-A	106	20	200	40.2	33.6	779	0.64	0.67	1.05	66	64	1.05
	H200L4-B	106	20	200	40.2	33.6	779	0.61	0.67	1.09	67	64	1.09
	H200L4-C	106	20	200	40.2	33.6	779	0.57	0.67	1.18	70	64	1.18
	H400L2-A	106	20	400	40.2	24.5	479	0.59	0.63	1.07	49	47	1.07
	H400L2-B	106	20	400	40.2	24.5	479	0.52	0.63	1.19	52	47	1.19
	H400L2-C	106	20	400	40.2	24.5	479	0.68	0.63	0.92	46	47	0.92
	H400L3-A	106	20	400	40.2	24.5	719	0.61	0.63	1.03	59	58	1.03
	H400L3-B	106	20	400	40.2	24.5	719	0.78	0.63	0.80	51	58	0.80
	H400L3-C	106	20	400	40.2	24.5	719	0.64	0.63	0.97	57	58	0.97
	H400L4-A	106	20	400	40.2	24.5	779	0.56	0.63	1.11	64	60	1.11

	H400L4-B	106	20	400	40.2	24.5	779	0.50	0.63	1.25	69	60	1.25
	H400L4-C	106	20	400	40.2	24.5	779	0.56	0.63	1.12	65	60	1.12
	H600L2-A	106	20	600	40.2	15.4	479	0.57	0.60	1.05	44	43	1.05
	H600L2-B	106	20	600	40.2	15.4	479	0.53	0.60	1.14	46	43	1.14
	H600L2-C	106	20	600	40.2	15.4	479	0.54	0.60	1.12	46	43	1.12
	H600L3-A	106	20	600	40.2	15.4	719	0.60	0.60	1.01	55	55	1.01
	H600L3-B	106	20	600	40.2	15.4	719	0.56	0.60	1.07	58	55	1.07
	H600L3-C	106	20	600	40.2	15.4	719	0.58	0.60	1.03	56	55	1.03
	H600L4-A	106	20	600	40.2	15.4	779	0.53	0.60	1.12	63	58	1.12
	H600L4-B	106	20	600	40.2	15.4	779	0.51	0.60	1.18	66	58	1.18
	H600L4-C	106	20	600	40.2	15.4	779	0.50	0.60	1.21	67	58	1.21
	H800L2-A	106	20	800	40.2	6.2	479	0.57	0.58	1.03	43	42	1.03
	H800L2-B	106	20	800	40.2	6.2	479	0.57	0.58	1.03	43	42	1.03
	H800L2-C	106	20	800	40.2	6.2	479	0.65	0.58	0.89	38	42	0.89
	H800L3-A	106	20	800	40.2	6.2	719	0.69	0.58	0.84	51	59	0.84
	H800L3-B	106	20	800	40.2	6.2	719	0.67	0.58	0.88	52	59	0.88
	H800L3-C	106	20	800	40.2	6.2	719	0.70	0.58	0.84	50	59	0.84
	H800L4-A	106	20	800	40.2	6.2	779	0.60	0.58	0.98	62	63	0.98
	H800L4-B	106	20	800	40.2	6.2	779	0.55	0.58	1.06	66	63	1.06
	H800L4-C	106	20	800	40.2	6.2	779	0.60	0.58	0.97	61	63	0.97
Lenwari *et al.* [5]	WP20-300-120-A-A	150	75	325	20.0	17.6	409	1.07	0.94	0.87	36	38	0.87
	WP20-300-120-A-B	150	75	325	20.0	17.6	409	0.78	0.94	1.21	43	38	1.21
	WP20-300-120-W-A	150	75	325	20.0	17.6	409	0.94	1.00	1.07	39	37	1.07
	WP20-300-120-W-B	150	75	325	20.0	17.6	409	0.82	1.00	1.22	42	37	1.22
	WP35-300-120-A-A	150	75	325	35.0	24.9	409	0.58	0.63	1.09	56	53	1.09
	WP35-300-120-A-B	150	75	325	35.0	24.9	409	0.58	0.63	1.09	56	53	1.09
	WP35-300-120-A-C	150	75	325	35.0	24.9	409	0.64	0.63	0.98	53	53	0.98
	WP35-300-120-W-A	150	75	325	35.0	24.9	409	0.70	0.74	1.06	50	49	1.06
	WP35-300-120-W-B	150	75	325	35.0	24.9	409	0.65	0.74	1.14	52	49	1.14
	WP50-300-120-A-A	150	75	325	50.0	34.6	409	0.46	0.49	1.05	70	68	1.05
	WP50-300-120-A-C	150	75	325	50.0	34.6	409	0.64	0.49	0.76	60	68	0.76
	WP50-300-120-W-A	150	75	325	50.0	34.6	409	0.45	0.57	1.27	71	63	1.27
	WP50-300-120-W-B	150	75	325	50.0	34.6	409	0.46	0.57	1.25	70	63	1.25
	WP50-300-120-W-C	150	75	325	50.0	34.6	409	0.54	0.57	1.06	65	63	1.06
	WP20-500-120-A-A	150	75	500	20.0	12.6	409	0.85	0.90	1.05	38	36	1.05
	WP20-500-120-A-B	150	75	500	20.0	12.6	409	0.80	0.90	1.13	40	36	1.13
	WP20-500-120-A-C	150	75	500	20.0	12.6	409	0.71	0.90	1.27	43	36	1.27
	WP20-500-120-W-A	150	75	500	20.0	12.6	409	0.85	1.00	1.18	38	34	1.18
	WP20-500-120-W-B	150	75	500	20.0	12.6	409	0.95	1.00	1.05	35	34	1.05
	WP20-500-120-W-C	150	75	500	20.0	12.6	409	0.79	1.00	1.26	40	34	1.26
	WP35-500-120-A-A	150	75	500	35.5	18.0	409	0.61	0.59	0.98	50	51	0.98
	WP35-500-120-A-B	150	75	500	35.5	18.0	409	0.61	0.59	0.97	50	51	0.97
	WP35-500-120-A-C	150	75	500	35.5	18.0	409	0.63	0.59	0.94	49	51	0.94
	WP35-500-120-W-A	150	75	500	35.5	18.0	409	0.68	0.70	1.03	47	46	1.03
	WP35-500-120-W-C	150	75	500	35.5	18.0	409	0.60	0.70	1.17	50	46	1.17
	WP50-500-120-A-B	150	75	500	50.0	24.7	409	0.51	0.46	0.91	59	63	0.91
	WP50-500-120-A-C	150	75	500	50.0	24.7	409	0.40	0.46	1.17	69	63	1.17
	WP50-500-120-W-A	150	75	500	50.0	24.7	409	0.45	0.55	1.21	64	57	1.21
	WP50-500-120-W-B	150	75	500	50.0	24.7	409	0.45	0.55	1.20	64	57	1.20
	WP50-500-120-W-C	150	75	500	50.0	24.7	409	0.47	0.55	1.17	63	57	1.17
	WP20-700-120-A-A	150	75	700	20.0	6.8	409	0.88	0.87	0.99	36	36	0.99
	WP20-700-120-A-C	150	75	700	20.0	6.8	409	0.79	0.87	1.09	39	36	1.09
	WP20-700-120-W-A	150	75	700	20.0	6.8	409	0.96	1.00	1.04	33	32	1.04
	WP20-700-120-W-B	150	75	700	20.0	6.8	409	1.07	1.00	0.93	31	32	0.93
	WP20-700-120-W-C	150	75	700	20.0	6.8	409	1.01	1.00	0.99	32	32	0.99
	WP35-700-120-A-A	150	75	700	35.0	9.6	409	0.61	0.58	0.95	48	49	0.95
	WP35-700-120-A-B	150	75	700	35.0	9.6	409	0.56	0.58	1.03	51	49	1.03
	WP35-700-120-A-C	150	75	700	35.0	9.6	409	0.67	0.58	0.87	44	49	0.87
	WP35-700-120-W-A	150	75	700	35.0	9.6	409	0.74	0.68	0.93	41	44	0.93
	WP35-700-120-W-B	150	75	700	35.0	9.6	409	0.70	0.68	0.97	43	44	0.97
	WP35-700-120-W-C	150	75	700	35.0	9.6	409	0.74	0.68	0.92	41	44	0.92
	WP50-700-120-A-A	150	75	700	50.0	13.4	409	0.44	0.45	1.02	61	60	1.02
	WP50-700-120-A-B	150	75	700	50.0	13.4	409	0.36	0.45	1.25	72	60	1.25
	WP50-700-120-A-C	150	75	700	50.0	13.4	409	0.42	0.45	1.07	63	60	1.07

	WP50-700-120-W-A	150	75	700	50.0	13.4	409	0.68	0.53	0.78	45	53	0.78
	WP50-700-120-W-B	150	75	700	50.0	13.4	409	0.67	0.53	0.79	45	53	0.79
	WP50-700-120-W-C	150	75	700	50.0	13.4	409	0.66	0.53	0.80	45	53	0.80
	WP20-700-180-A-A	150	75	700	20.0	6.8	409	0.89	0.87	0.98	36	36	0.98
	WP20-700-180-A-A	150	75	700	20.0	6.8	409	0.77	0.87	1.13	40	36	1.13
	WP20-700-180-A-A	150	75	700	20.0	6.8	409	0.92	0.87	0.94	34	36	0.94
	WP20-700-180-W-A	150	75	700	20.0	6.8	409	0.99	1.00	1.01	33	32	1.01
	WP20-700-180-W-A	150	75	700	20.0	6.8	409	1.06	1.00	0.94	31	32	0.94
	WP20-700-180-W-A	150	75	700	20.0	6.8	409	1.04	1.00	0.96	31	32	0.96
	WP35-700-180-A-A	150	75	700	35.0	9.6	409	0.62	0.58	0.93	47	49	0.93
	WP35-700-180-A-A	150	75	700	35.0	9.6	409	0.66	0.58	0.88	45	49	0.88
	WP35-700-180-A-A	150	75	700	35.0	9.6	409	0.68	0.58	0.86	44	49	0.86
	WP35-700-180-W-A	150	75	700	35.0	9.6	409	0.74	0.68	0.93	41	44	0.93
	WP35-700-180-W-A	150	75	700	35.0	9.6	409	0.77	0.68	0.88	40	44	0.88
	WP35-700-180-W-A	150	75	700	35.0	9.6	409	0.86	0.68	0.79	36	44	0.79
	WP50-700-180-A-A	150	75	700	50.0	13.4	409	0.41	0.45	1.08	64	60	1.08
	WP50-700-180-A-A	150	75	700	50.0	13.4	409	0.45	0.45	1.01	61	60	1.01
	WP50-700-180-A-A	150	75	700	50.0	13.4	409	0.40	0.45	1.11	66	60	1.11
	WP50-700-180-W-A	150	75	700	50.0	13.4	409	0.52	0.53	1.01	54	53	1.01
	WP50-700-180-W-A	150	75	700	50.0	13.4	409	0.54	0.53	0.98	53	53	0.98
Bisby *et al.* [4]	W-300-120-A	100	50	300	28.0	22.2	579	0.65	0.74	1.15	63	58	1.15
	W-300-120-B	100	50	300	28.0	22.2	579	0.68	0.74	1.09	61	58	1.09
	W-300-120-C	100	50	300	28.0	22.2	579	0.72	0.74	1.04	59	58	1.04
	W-500-120-A	100	50	500	28.0	15.2	579	0.69	0.71	1.03	58	57	1.03
	W-500-120-B	100	50	500	28.0	15.2	579	0.92	0.71	0.76	47	57	0.76
	W-500-120-C	100	50	500	28.0	15.2	579	0.70	0.71	1.01	57	57	1.01
	W-686-120-A	100	50	686	28.0	8.7	579	0.83	0.68	0.82	50	59	0.82
	W-686-120-B	100	50	686	28.0	8.7	579	0.74	0.68	0.92	55	59	0.92
	W-686-120-C	100	50	686	28.0	8.7	579	0.85	0.68	0.80	49	59	0.80
	W-686-240-A	100	50	686	28.0	8.7	579	0.87	0.68	0.78	48	59	0.78
	W-686-240-B	100	50	686	28.0	8.7	579	0.74	0.68	0.92	55	59	0.92
	W-686-240-C	100	50	686	28.0	8.7	579	0.83	0.68	0.82	50	59	0.82

Table 2

Table. 2. Comparison of experimental and obtained results of α_T and $\varepsilon_{cu,T}$

Test ID		b (mm)	r (mm)	T (°C)	f_{c0} (MPa)	f_{c0}^{T} (MPa)	K_L (MPa)	α_T^{Exp}	α_T^{Ana}	$\alpha_T^{Ana}/\alpha_T^{Exp}$	$\varepsilon_{cu,T}^{Exp}$	$\varepsilon_{cu,T}^{Ana}$	$\varepsilon_{cu,T}^{Ana}/\varepsilon_{cu,T}^{Exp}$
Ouyang et al. [6]	T200-L2-1	150	75	200	45.1	37.4	349	2.0	2.1	1.09	0.008	0.007	0.92
	T200-L2-2	150	75	200	45.1	37.4	349	2.0	2.1	1.09	0.008	0.007	0.92
	T200-L2-3	150	75	200	45.1	37.4	349	2.4	2.1	0.90	0.007	0.007	1.11
	T200-L3-1	150	75	200	45.1	37.4	524	2.5	2.1	0.87	0.008	0.009	1.15
	T200-L3-2	150	75	200	45.1	37.4	524	1.8	2.1	1.20	0.011	0.009	0.83
	T200-L3-3	150	75	200	45.1	37.4	524	2.2	2.1	0.97	0.009	0.009	1.03
	T200-L4-1	150	75	200	45.1	37.4	568	1.8	2.1	1.21	0.011	0.010	0.83
	T200-L4-2	150	75	200	45.1	37.4	568	1.8	2.1	1.18	0.011	0.010	0.85
	T200-L4-3	150	75	200	45.1	37.4	568	1.9	2.1	1.13	0.011	0.010	0.88
	T400-L2-1	150	75	400	45.1	27.2	349	3.2	3.3	1.03	0.009	0.009	0.97
	T400-L2-2	150	75	400	45.1	27.2	349	4.4	3.3	0.75	0.006	0.009	1.33
	T400-L2-3	150	75	400	45.1	27.2	349	4.7	3.3	0.70	0.006	0.009	1.42
	T400-L3-1	150	75	400	45.1	27.2	524	4.7	3.3	0.71	0.008	0.011	1.40
	T400-L3-2	150	75	400	45.1	27.2	524	3.8	3.3	0.87	0.009	0.011	1.15
	T400-L3-3	150	75	400	45.1	27.2	524	3.9	3.3	0.85	0.009	0.011	1.18
	T400-L4-1	150	75	400	45.1	27.2	568	2.6	3.3	1.27	0.014	0.011	0.79
	T400-L4-2	150	75	400	45.1	27.2	568	3.2	3.3	1.03	0.011	0.011	0.97
	T400-L4-3	150	75	400	45.1	27.2	568	3.0	3.3	1.11	0.012	0.011	0.90
	T600-L2-1	150	75	600	45.1	17.1	349	5.7	5.0	0.86	0.011	0.013	1.16
	T600-L2-2	150	75	600	45.1	17.1	349	5.4	5.0	0.91	0.011	0.013	1.10
	T600-L2-3	150	75	600	45.1	17.1	349	4.7	5.0	1.06	0.013	0.013	0.95
	T600-L3-1	150	75	600	45.1	17.1	524	4.8	5.0	1.03	0.016	0.016	0.98
	T600-L3-2	150	75	600	45.1	17.1	524	4.7	5.0	1.06	0.017	0.016	0.94
	T600-L3-3	150	75	600	45.1	17.1	524	5.1	5.0	0.97	0.015	0.016	1.03
	T600-L4-1	150	75	600	45.1	17.1	568	4.2	5.0	1.18	0.019	0.016	0.85
	T600-L4-2	150	75	600	45.1	17.1	568	3.9	5.0	1.28	0.021	0.016	0.78
	T600-L4-3	150	75	600	45.1	17.1	568	4.4	5.0	1.11	0.018	0.016	0.90
	T800-L2-1	150	75	800	45.1	7.0	349	11.5	12.4	1.07	0.016	0.015	0.93
	T800-L2-2	150	75	800	45.1	7.0	349	10.8	12.4	1.15	0.018	0.015	0.87
	T800-L2-3	150	75	800	45.1	7.0	349	10.2	12.4	1.21	0.018	0.015	0.83
	T800-L3-1	150	75	800	45.1	7.0	524	9.7	12.4	1.28	0.025	0.019	0.78
	T800-L3-2	150	75	800	45.1	7.0	524	12.5	12.4	0.99	0.019	0.019	1.01
	T800-L3-3	150	75	800	45.1	7.0	524	11.3	12.4	1.09	0.021	0.019	0.91
	T800-L4-1	150	75	800	45.1	7.0	568	12.0	12.4	1.03	0.021	0.020	0.97
	T800-L4-2	150	75	800	45.1	7.0	568	9.1	12.4	1.36	0.027	0.020	0.74
	T800-L4-3	150	75	800	45.1	7.0	568	10.0	12.4	1.24	0.025	0.020	0.81
Song et al. [7]	H200L2-A	106	20	200	40.2	33.6	479	3.1	2.1	0.69	0.005	0.008	1.44
	H200L2-B	106	20	200	40.2	33.6	479	2.8	2.1	0.76	0.006	0.008	1.31
	H200L2-C	106	20	200	40.2	33.6	479	2.5	2.1	0.84	0.007	0.008	1.19
	H200L3-A	106	20	200	40.2	33.6	719	1.9	2.1	1.13	0.011	0.010	0.88
	H200L3-B	106	20	200	40.2	33.6	719	2.6	2.1	0.82	0.008	0.010	1.22
	H200L3-C	106	20	200	40.2	33.6	719	2.0	2.1	1.06	0.010	0.010	0.94
	H200L4-A	106	20	200	40.2	33.6	779	2.0	2.1	1.08	0.011	0.010	0.92
	H200L4-B	106	20	200	40.2	33.6	779	1.5	2.1	1.42	0.015	0.010	0.70
	H200L4-C	106	20	200	40.2	33.6	779	1.7	2.1	1.25	0.013	0.010	0.80
	H400L2-A	106	20	400	40.2	24.5	479	4.4	3.3	0.76	0.007	0.009	1.31
	H400L2-B	106	20	400	40.2	24.5	479	4.2	3.3	0.79	0.007	0.009	1.27
	H400L2-C	106	20	400	40.2	24.5	479	5.2	3.3	0.64	0.006	0.009	1.57
	H400L3-A	106	20	400	40.2	24.5	719	3.0	3.3	1.10	0.013	0.012	0.91
	H400L3-B	106	20	400	40.2	24.5	719	3.2	3.3	1.06	0.013	0.012	0.95
	H400L3-C	106	20	400	40.2	24.5	719	3.3	3.3	1.02	0.012	0.012	0.98
	H400L4-A	106	20	400	40.2	24.5	779	3.0	3.3	1.11	0.014	0.012	0.90
	H400L4-B	106	20	400	40.2	24.5	779	3.0	3.3	1.12	0.014	0.012	0.89

	H400L4-C	106	20	400	40.2	24.5	779	2.6	3.3	1.28	0.016	0.012	0.78
	H600L2-A	106	20	600	40.2	15.4	479	5.1	5.0	0.97	0.015	0.015	1.03
	H600L2-B	106	20	600	40.2	15.4	479	6.2	5.0	0.79	0.012	0.015	1.26
	H600L2-C	106	20	600	40.2	15.4	479	4.8	5.0	1.02	0.015	0.015	0.98
	H600L3-A	106	20	600	40.2	15.4	719	5.1	5.0	0.97	0.018	0.019	1.03
	H600L3-B	106	20	600	40.2	15.4	719	5.9	5.0	0.84	0.016	0.019	1.20
	H600L3-C	106	20	600	40.2	15.4	719	5.5	5.0	0.91	0.017	0.019	1.10
	H600L4-A	106	20	600	40.2	15.4	779	5.6	5.0	0.88	0.017	0.020	1.14
	H600L4-B	106	20	600	40.2	15.4	779	4.9	5.0	1.00	0.020	0.020	1.00
	H600L4-C	106	20	600	40.2	15.4	779	4.6	5.0	1.08	0.021	0.020	0.93
	H800L2-A	106	20	800	40.2	6.2	479	13.3	12.4	0.93	0.021	0.022	1.07
	H800L2-B	106	20	800	40.2	6.2	479	15.8	12.4	0.79	0.017	0.022	1.27
	H800L2-C	106	20	800	40.2	6.2	479	14.7	12.4	0.84	0.019	0.022	1.18
	H800L3-A	106	20	800	40.2	6.2	719	13.8	12.4	0.90	0.025	0.028	1.11
	H800L3-B	106	20	800	40.2	6.2	719	13.3	12.4	0.93	0.026	0.028	1.07
	H800L3-C	106	20	800	40.2	6.2	719	14.5	12.4	0.85	0.024	0.028	1.17
	H800L4-A	106	20	800	40.2	6.2	779	12.1	12.4	1.02	0.030	0.029	0.98
	H800L4-B	106	20	800	40.2	6.2	779	12.0	12.4	1.03	0.030	0.029	0.97
	H800L4-C	106	20	800	40.2	6.2	779	13.1	12.4	0.94	0.028	0.029	1.06
	WP20-300-120-A-A	150	75	325	20.0	17.6	409	3.1	3.1	1.00	0.008	0.008	1.00
	WP20-300-120-A-B	150	75	325	20.0	17.6	409	2.6	3.1	1.20	0.010	0.008	0.83
	WP20-300-120-W-A	150	75	325	20.0	17.6	409	2.2	2.1	0.93	0.012	0.012	1.08
	WP20-300-120-W-B	150	75	325	20.0	17.6	409	2.1	2.1	0.99	0.012	0.012	1.01
	WP35-300-120-A-A	150	75	325	35.0	24.9	409	1.6	3.1	1.99	0.014	0.007	0.50
	WP35-300-120-A-B	150	75	325	35.0	24.9	409	1.7	3.1	1.82	0.013	0.007	0.55
	WP35-300-120-A-C	150	75	325	35.0	24.9	409	1.4	3.1	2.16	0.015	0.007	0.46
	WP35-300-120-W-A	150	75	325	35.0	24.9	409	2.6	2.1	0.79	0.008	0.011	1.27
	WP35-300-120-W-B	150	75	325	35.0	24.9	409	1.4	2.1	1.44	0.015	0.011	0.70
	WP35-300-120-W-C	150	75	325	35.0	24.9	409	1.5	2.1	1.42	0.015	0.011	0.71
	WP20-500-120-A-A	150	75	500	20.0	12.6	409	2.8	3.8	1.34	0.019	0.014	0.74
	WP20-500-120-A-B	150	75	500	20.0	12.6	409	3.0	3.8	1.24	0.018	0.014	0.80
	WP20-500-120-A-C	150	75	500	20.0	12.6	409	3.3	3.8	1.12	0.016	0.014	0.89
	WP20-500-120-W-A	150	75	500	20.0	12.6	409	2.8	2.5	0.89	0.019	0.021	1.12
	WP20-500-120-W-B	150	75	500	20.0	12.6	409	2.7	2.5	0.92	0.020	0.021	1.09
	WP35-500-120-A-A	150	75	500	35.5	18.0	409	3.5	3.8	1.09	0.012	0.011	0.92
	WP35-500-120-A-B	150	75	500	35.5	18.0	409	3.3	3.8	1.12	0.012	0.011	0.89
	WP35-500-120-A-C	150	75	500	35.5	18.0	409	2.7	3.8	1.38	0.015	0.011	0.73
	WP35-500-120-W-A	150	75	500	35.5	18.0	409	3.3	2.5	0.75	0.012	0.017	1.34
	WP35-500-120-W-C	150	75	500	35.5	18.0	409	2.8	2.5	0.89	0.015	0.017	1.13
	WP50-500-120-W-A	150	75	500	50.0	24.7	409	2.5	2.5	0.99	0.013	0.013	1.01
	WP50-500-120-W-B	150	75	500	50.0	24.7	409	2.1	2.5	1.20	0.016	0.013	0.84
Lenwari et al. [5]	WP50-500-120-W-C	150	75	500	50.0	24.7	409	3.1	2.5	0.80	0.011	0.013	1.24
	WP20-700-120-A-A	150	75	700	20.0	6.8	409	8.0	7.6	0.95	0.019	0.020	1.06
	WP20-700-120-A-C	150	75	700	20.0	6.8	409	6.4	7.6	1.19	0.024	0.020	0.84
	WP20-700-120-W-A	150	75	700	20.0	6.8	409	4.3	5.0	1.17	0.036	0.030	0.86
	WP20-700-120-W-B	150	75	700	20.0	6.8	409	6.2	5.0	0.81	0.025	0.030	1.23
	WP20-700-120-W-C	150	75	700	20.0	6.8	409	5.5	5.0	0.91	0.028	0.030	1.10
	WP35-700-120-A-A	150	75	700	35.0	9.6	409	6.8	7.6	1.12	0.016	0.014	0.89
	WP35-700-120-A-B	150	75	700	35.0	9.6	409	8.6	7.6	0.88	0.013	0.014	1.13
	WP35-700-120-A-C	150	75	700	35.0	9.6	409	7.8	7.6	0.97	0.014	0.014	1.03
	WP35-700-120-W-A	150	75	700	35.0	9.6	409	3.1	5.0	1.64	0.036	0.022	0.61
	WP35-700-120-W-B	150	75	700	35.0	9.6	409	3.2	5.0	1.58	0.034	0.022	0.63
	WP35-700-120-W-C	150	75	700	35.0	9.6	409	3.7	5.0	1.36	0.030	0.022	0.74
	WP50-700-120-A-A	150	75	700	50.0	13.4	409	9.7	7.6	0.78	0.008	0.011	1.28
	WP50-700-120-A-B	150	75	700	50.0	13.4	409	8.4	7.6	0.90	0.010	0.011	1.11
	WP50-700-120-A-C	150	75	700	50.0	13.4	409	10.4	7.6	0.73	0.008	0.011	1.36
	WP50-700-120-W-A	150	75	700	50.0	13.4	409	5.8	5.0	0.86	0.014	0.016	1.16
	WP50-700-120-W-B	150	75	700	50.0	13.4	409	6.0	5.0	0.83	0.014	0.016	1.20
	WP50-700-120-W-C	150	75	700	50.0	13.4	409	5.8	5.0	0.87	0.014	0.016	1.15
	WP20-700-180-A-A	150	75	700	20.0	6.8	409	8.4	7.6	0.90	0.018	0.020	1.11
	WP20-700-180-A-A	150	75	700	20.0	6.8	409	7.4	7.6	1.03	0.021	0.020	0.97
	WP20-700-180-A-A	150	75	700	20.0	6.8	409	8.1	7.6	0.94	0.019	0.020	1.06
	WP20-700-180-W-A	150	75	700	20.0	6.8	409	4.8	5.0	1.04	0.032	0.030	0.96
	WP20-700-180-W-A	150	75	700	20.0	6.8	409	4.8	5.0	1.04	0.032	0.030	0.96

	WP20-700-180-W-A	150	75	700	20.0	6.8	409	5.9	5.0	0.85	0.026	0.030	1.17
	WP35-700-180-A-A	150	75	700	35.0	9.6	409	5.7	7.6	1.34	0.019	0.014	0.74
	WP35-700-180-A-A	150	75	700	35.0	9.6	409	8.9	7.6	0.86	0.012	0.014	1.17
	WP35-700-180-A-A	150	75	700	35.0	9.6	409	6.2	7.6	1.23	0.018	0.014	0.81
	WP35-700-180-W-A	150	75	700	35.0	9.6	409	4.4	5.0	1.13	0.025	0.022	0.88
	WP35-700-180-W-A	150	75	700	35.0	9.6	409	4.6	5.0	1.09	0.024	0.022	0.92
	WP35-700-180-W-A	150	75	700	35.0	9.6	409	4.7	5.0	1.07	0.023	0.022	0.94
	WP50-700-180-A-A	150	75	700	50.0	13.4	409	6.8	7.6	1.12	0.012	0.011	0.89
	WP50-700-180-A-A	150	75	700	50.0	13.4	409	7.7	7.6	0.98	0.011	0.011	1.02
	WP50-700-180-A-A	150	75	700	50.0	13.4	409	6.3	7.6	1.20	0.013	0.011	0.83
	WP50-700-180-W-A	150	75	700	50.0	13.4	409	5.8	5.0	0.87	0.014	0.016	1.15
	WP50-700-180-W-A	150	75	700	50.0	13.4	409	4.8	5.0	1.05	0.017	0.016	0.95
Bisby et al. [4]	W-300-120-A	100	50	300	28.0	22.2	579	2.0	3.0	1.52	0.013	0.009	0.66
	W-300-120-B	100	50	300	28.0	22.2	579	2.0	3.0	1.53	0.013	0.009	0.65
	W-300-120-C	100	50	300	28.0	22.2	579	2.0	3.0	1.54	0.013	0.009	0.65
	W-500-120-A	100	50	500	28.0	15.2	579	3.6	3.8	1.04	0.015	0.015	0.96
	W-500-120-B	100	50	500	28.0	15.2	579	3.2	3.8	1.17	0.017	0.015	0.86
	W-500-120-C	100	50	500	28.0	15.2	579	4.1	3.8	0.92	0.014	0.015	1.09
	W-686-120-A	100	50	686	28.0	8.7	579	7.6	7.1	0.94	0.018	0.020	1.06
	W-686-120-B	100	50	686	28.0	8.7	579	10.2	7.1	0.70	0.014	0.020	1.44
	W-686-120-C	100	50	686	28.0	8.7	579	7.8	7.1	0.91	0.018	0.020	1.10
	W-686-240-A	100	50	686	28.0	8.7	579	7.3	7.1	0.98	0.019	0.020	1.02
	W-686-240-B	100	50	686	28.0	8.7	579	8.0	7.1	0.90	0.018	0.020	1.12
	W-686-240-C	100	50	686	28.0	8.7	579	8.8	7.1	0.81	0.016	0.020	1.23

Table 3

Table. 3. Comparison of experimental and obtained results of ψ_T and $f_{ctr,T}$

Test ID		b (mm)	r (mm)	T (°C)	f_{c0} (MPa)	f_{c0}^{T} (MPa)	K_L (MPa)	ψ_T^{Exp}	ψ_T^{Ana}	$\psi_T^{Ana}/\psi_T^{Exp}$	$f_{ctr,T}^{Exp}$	$f_{ctr,T}^{Ana}$	$f_{ctr,T}^{Ana}/f_{ctr,T}^{Exp}$
Ouyang et al. [6]	T200-L2-1	150	75	200	45.1	37.4	349	2.20	1.87	0.85	66	56	0.85
	T200-L2-2	150	75	200	45.1	37.4	349	2.20	1.87	0.85	66	56	0.85
	T200-L2-3	150	75	200	45.1	37.4	349	2.20	1.87	0.85	66	56	0.85
	T200-L3-1	150	75	200	45.1	37.4	524	2.30	2.12	0.92	67	62	0.92
	T200-L3-2	150	75	200	45.1	37.4	524	2.30	2.12	0.92	67	62	0.92
	T200-L3-3	150	75	200	45.1	37.4	524	2.30	2.12	0.92	67	62	0.92
	T200-L4-1	150	75	200	45.1	37.4	568	2.60	2.17	0.83	76	63	0.83
	T200-L4-2	150	75	200	45.1	37.4	568	2.60	2.17	0.83	76	63	0.83
	T200-L4-3	150	75	200	45.1	37.4	568	2.60	2.17	0.83	76	63	0.83
	T400-L2-1	150	75	400	45.1	27.2	349	1.95	1.64	0.84	63	53	0.84
	T400-L2-2	150	75	400	45.1	27.2	349	1.95	1.64	0.84	63	53	0.84
	T400-L2-3	150	75	400	45.1	27.2	349	1.95	1.64	0.84	63	53	0.84
	T400-L3-1	150	75	400	45.1	27.2	524	2.15	1.85	0.86	70	61	0.86
	T400-L3-2	150	75	400	45.1	27.2	524	2.15	1.85	0.86	70	61	0.86
	T400-L3-3	150	75	400	45.1	27.2	524	2.15	1.85	0.86	70	61	0.86
	T400-L4-1	150	75	400	45.1	27.2	568	2.25	1.90	0.84	74	63	0.84
	T400-L4-2	150	75	400	45.1	27.2	568	2.25	1.90	0.84	74	63	0.84
	T400-L4-3	150	75	400	45.1	27.2	568	2.25	1.90	0.84	74	63	0.84
	T600-L2-1	150	75	600	45.1	17.1	349	1.33	1.32	0.99	39	38	0.99
	T600-L2-2	150	75	600	45.1	17.1	349	1.33	1.32	0.99	39	38	0.99
	T600-L2-3	150	75	600	45.1	17.1	349	1.33	1.32	0.99	39	38	0.99
	T600-L3-1	150	75	600	45.1	17.1	524	1.35	1.49	1.11	42	47	1.11
	T600-L3-2	150	75	600	45.1	17.1	524	1.35	1.49	1.11	42	47	1.11
	T600-L3-3	150	75	600	45.1	17.1	524	1.35	1.49	1.11	42	47	1.11
	T600-L4-1	150	75	600	45.1	17.1	568	1.27	1.53	1.20	41	49	1.20
	T600-L4-2	150	75	600	45.1	17.1	568	1.27	1.53	1.20	41	49	1.20
	T600-L4-3	150	75	600	45.1	17.1	568	1.27	1.53	1.20	41	49	1.20
	T800-L2-1	150	75	800	45.1	7.0	349	1.03	1.00	0.97	35	34	0.97
	T800-L2-2	150	75	800	45.1	7.0	349	1.03	1.00	0.97	35	34	0.97
	T800-L2-3	150	75	800	45.1	7.0	349	1.03	1.00	0.97	35	34	0.97
	T800-L3-1	150	75	800	45.1	7.0	524	1.04	1.09	1.05	42	44	1.05
	T800-L3-2	150	75	800	45.1	7.0	524	1.04	1.09	1.05	42	44	1.05
	T800-L3-3	150	75	800	45.1	7.0	524	1.04	1.09	1.05	42	44	1.05
	T800-L4-1	150	75	800	45.1	7.0	568	1.10	1.11	1.01	46	46	1.01
	T800-L4-2	150	75	800	45.1	7.0	568	1.10	1.11	1.01	46	46	1.01
	T800-L4-3	150	75	800	45.1	7.0	568	1.10	1.11	1.01	46	46	1.01
Song et al. [7]	H200L2-A	106	20	200	40.2	33.6	479	2.31	2.50	1.08	52	57	1.08
	H200L2-B	106	20	200	40.2	33.6	479	2.31	2.50	1.08	52	57	1.08
	H200L2-C	106	20	200	40.2	33.6	479	2.31	2.50	1.08	52	57	1.08
	H200L3-A	106	20	200	40.2	33.6	719	2.72	2.83	1.04	58	61	1.04
	H200L3-B	106	20	200	40.2	33.6	719	2.72	2.83	1.04	58	61	1.04
	H200L3-C	106	20	200	40.2	33.6	719	2.72	2.83	1.04	58	61	1.04
	H200L4-A	106	20	200	40.2	33.6	779	2.74	2.90	1.06	58	62	1.06
	H200L4-B	106	20	200	40.2	33.6	779	2.74	2.90	1.06	58	62	1.06
	H200L4-C	106	20	200	40.2	33.6	779	2.74	2.90	1.06	58	62	1.06
	H400L2-A	106	20	400	40.2	24.5	479	2.04	2.19	1.07	47	50	1.07
	H400L2-B	106	20	400	40.2	24.5	479	2.04	2.19	1.07	47	50	1.07
	H400L2-C	106	20	400	40.2	24.5	479	2.04	2.19	1.07	47	50	1.07
	H400L3-A	106	20	400	40.2	24.5	719	2.35	2.47	1.05	54	57	1.05
	H400L3-B	106	20	400	40.2	24.5	719	2.35	2.47	1.05	54	57	1.05
	H400L3-C	106	20	400	40.2	24.5	719	2.35	2.47	1.05	54	57	1.05
	H400L4-A	106	20	400	40.2	24.5	779	2.45	2.53	1.03	57	58	1.03

	H400L4-B	106	20	400	40.2	24.5	779	2.45	2.53	1.03	57	58	1.03
	H400L4-C	106	20	400	40.2	24.5	779	2.45	2.53	1.03	57	58	1.03
	H600L2-A	106	20	600	40.2	15.4	479	1.85	1.77	0.95	35	34	0.95
	H600L2-B	106	20	600	40.2	15.4	479	1.85	1.77	0.95	35	34	0.95
	H600L2-C	106	20	600	40.2	15.4	479	1.85	1.77	0.95	35	34	0.95
	H600L3-A	106	20	600	40.2	15.4	719	2.17	1.99	0.92	44	40	0.92
	H600L3-B	106	20	600	40.2	15.4	719	2.17	1.99	0.92	44	40	0.92
	H600L3-C	106	20	600	40.2	15.4	719	2.17	1.99	0.92	44	40	0.92
	H600L4-A	106	20	600	40.2	15.4	779	2.20	2.04	0.93	45	42	0.93
	H600L4-B	106	20	600	40.2	15.4	779	2.20	2.04	0.93	45	42	0.93
	H600L4-C	106	20	600	40.2	15.4	779	2.20	2.04	0.93	45	42	0.93
	H800L2-A	106	20	800	40.2	6.2	479	1.72	1.29	0.75	30	22	0.75
	H800L2-B	106	20	800	40.2	6.2	479	1.72	1.29	0.75	30	22	0.75
	H800L2-C	106	20	800	40.2	6.2	479	1.72	1.29	0.75	30	22	0.75
	H800L3-A	106	20	800	40.2	6.2	719	1.65	1.45	0.88	34	30	0.88
	H800L3-B	106	20	800	40.2	6.2	719	1.65	1.45	0.88	34	30	0.88
	H800L3-C	106	20	800	40.2	6.2	719	1.65	1.45	0.88	34	30	0.88
	H800L4-A	106	20	800	40.2	6.2	779	1.75	1.49	0.85	37	31	0.85
	H800L4-B	106	20	800	40.2	6.2	779	1.75	1.49	0.85	37	31	0.85
	H800L4-C	106	20	800	40.2	6.2	779	1.75	1.49	0.85	37	31	0.85
Lenwari et al. [5]	WP35-300-120-A-A	150	75	325	35.0	24.9	409	1.68	1.83	1.09	47	51	1.09
	WP35-300-120-A-B	150	75	325	35.0	24.9	409	1.68	1.83	1.09	47	51	1.09
	WP35-300-120-A-C	150	75	325	35.0	24.9	409	1.68	1.83	1.09	47	51	1.09
	WP35-500-120-A-A	150	75	500	35.5	18.0	409	1.74	1.56	0.90	41	37	0.90
	WP35-500-120-A-B	150	75	500	35.5	18.0	409	1.74	1.56	0.90	41	37	0.90
	WP35-500-120-A-C	150	75	500	35.5	18.0	409	1.74	1.56	0.90	41	37	0.90
	WP35-700-180-A-A	150	75	700	35.0	9.6	409	1.10	1.20	1.09	30	32	1.09
	WP35-700-180-A-A	150	75	700	35.0	9.6	409	1.10	1.20	1.09	30	32	1.09
	WP35-700-180-A-A	150	75	700	35.0	9.6	409	1.10	1.20	1.09	30	32	1.09
Bisby et al. [4]	W-300-120-A	100	50	300	28.0	22.2	579	1.68	2.06	1.23	38	46	1.23
	W-300-120-B	100	50	300	28.0	22.2	579	1.68	2.06	1.23	38	46	1.23
	W-300-120-C	100	50	300	28.0	22.2	579	1.68	2.06	1.23	38	46	1.23
	W-500-120-A	100	50	500	28.0	15.2	579	1.72	1.73	1.01	34	34	1.01
	W-500-120-B	100	50	500	28.0	15.2	579	1.72	1.73	1.01	34	34	1.01
	W-500-120-C	100	50	500	28.0	15.2	579	1.72	1.73	1.01	34	34	1.01
	W-686-120-A	100	50	686	28.0	8.7	579	1.35	1.36	1.01	32	33	1.01
	W-686-120-B	100	50	686	28.0	8.7	579	1.35	1.36	1.01	32	33	1.01
	W-686-120-C	100	50	686	28.0	8.7	579	1.35	1.36	1.01	32	33	1.01

Table A1

Table A1. Summary of the test database collected for f_{cu} of FCCC

Confinement arrangement	**Number of datasets**		f_{c0} **range (MPa)**	$\frac{f_{cu}}{f_{c0}}$ **range**	L **range (mm)**	b **range (mm)**	E_f **range (GPa)**	ε_{fu} **range**
FCCC	**1517**	Min.	6.6	1.05	100	50	9.5	0.004
		Max.	204.0	6.90	915	305	657	0.100
		MV	47.3	2.06	301	144	174	0.024
		CoV	0.700	0.414	0.352	0.295	0.614	0.801

Table A2

Table A2. Summary of the test database collected for f_{cu} of FCSC

Confinement arrangement	Number of datasets		f_{c0} range (MPa)	$\frac{f_{cu}}{f_{c0}}$ range	L range (mm)	b range (mm)	E_f range (GPa)	ε_{fu} range	R_b [a]
FCSC	256	Min.	8.7	1.05	200	100	9.5	0.009	0.07
		Max.	77.2	4.32	1200	400	260	0.093	0.80
		MV	32.1	1.70	401	170	175	0.026	0.36
		CoV	0.404	0.341	0.395	0.305	0.530	0.793	0.527

a: $R_b = 2r/b$ represents the corner radius ratio.

Table A3

Table A3. Summary of the test database collected for $f_{cu,T}$ of FCHCC/FCHSC.

Confinement arrangement	Number of datasets		f_{c0}^{T} [a] range (MPa)	$\frac{f_{cu,T}}{f_{c0}}$ range	L range (mm)	b range (mm)	E_f range (GPa)	ε_{fu} range	R_b [b]	T_m [c]
FCHCC/FCHSC	**141**	Min.	6.24	1.50	200	100	105	0.017	0.38	200
		Max.	37.4	13.4	300	150	241	0.022	1	800
		MV	17.5	4.21	291	135	170	0.020	0.84	539
		CoV	0.543	0.579	0.096	0.161	0.379	0.101	0.323	0.362

a: Deteriorated compressive strength (f_{c0}^{T}) was calculated based on Eq. (C-1)

b: $R_b = 2r/b$ represents the corner radius ratio.

c: T_m represents the maximum exposure temperature based on the heating scheme (Fig. 1b).

Table A4

Table A4. Summary of the test database collected for ε_{cu} of FCCC

Confinement arrangement	Number of datasets		f_{c0} range (MPa)	$\frac{\varepsilon_{cu}}{\varepsilon_{c0}}$ range	L range (mm)	b range (mm)	E_f range (GPa)	ε_{fu} range
FCCC	1462	Min.	6.6	1.23	100	50	9.5	0.004
		Max.	204.0	95.2	915	305	657	0.100
		MV	47.9	10.4	301	145	171	0.024
		CoV	0.694	0.889	0.353	0.295	0.622	0.804

Table A5

Table A5. Summary of the test database collected for ε_{cu} of FCSC

Confinement arrangement	**Number of datasets**		f_{c0} **range (MPa)**	$\frac{\varepsilon_{cu}}{\varepsilon_{c0}}$ **range**	L **range (mm)**	b **range (mm)**	E_f **range (GPa)**	ε_{fu} **range**	R_b
FCSC	**246**	Min.	8.7	1.76	200	100	9.5	0.009	0.07
		Max.	77.2	73.0	1200	400	260	0.093	0.80
		MV	32.3	11.5	405	169	176	0.026	0.37
		CoV	0.406	0.966	0.396	0.310	0.529	0.804	0.530

Table A6

Table A6. Summary of the test database collected for $\varepsilon_{cu,T}$ of FCHCC/FCHSC.

Confinement arrangement	Number of datasets		f_{c0}^{T} range (MPa)	$\frac{\varepsilon_{cu,T}}{\varepsilon_{c0}^{T}}$ [a] range	L range (mm)	b range (mm)	E_f range (GPa)	ε_{fu} range	R_b	T_m
FCHCC/FCHSC	**141**	Min.	6.24	1.01	200	100	105	0.017	0.38	200
		Max.	37.4	5.61	300	150	241	0.022	1	800
		MV	17.5	2.83	291	135	170	0.020	0.84	539
		CoV	0.543	0.316	0.096	0.161	0.379	0.101	0.323	0.362

a: Strain (ε_{c0}^{T}) corresponding to f_{c0}^{T} was calculated based on Eq. (C-4)